NOISE DETECTION AND TRANSPORT MEASUREMENTS OF SPIN VALVE SYSTEMS

A DISSERTATION
SUBMITTED TO THE FACULTY OF THE GRADUATE SCHOOL
OF THE UNIVERSITY OF MINNESOTA
BY

FENG GUO

IN PARTIAL FULFILLMENT OF THE REQUIREMENTS
FOR THE DEGREE OF
DOCTOR OF PHILOSOPHY

ADVISER: E. DAN DAHLBERG

AUGUST 2011

Acknowledgements

All the work I have achieved and presented in this dissertation results from the support of my adviser, friends, colleagues, and of course my family.

I want to thank my adviser Dan Dahlberg for his guidance and for being a great mentor. I am extremely grateful to Greg McKusky for teaching me how to make tunnel junctions among many other fabrication techniques; to Tanner Schulz for the encouragements, support and sharing all the ups and downs in graduate school; to Dan Endean who carefully read and polished this thesis. My appreciation also goes to: Barry, Bern, Joe and Jimmy. Everyone in the group makes the lab a pleasant working environment by simply being wonderful and supportive. I am also very proud of being a member of the sub-basement (experimental condensed matter physics) community. I thank Allen Goldman's group and Paul Crowell's group and all other student colleagues. I feel lucky to have worked and lived with these brilliant fellow graduate students and some of them have become good friends of mine over the years. So many great memories came from this particular place and this particular building! They are absolutely the treasures of my life.

Besides my adviser, I need to particularly thank Prof. Paul Crowell and Prof. Randy Victora for many helpful discussions and showing me the passion for physics, which is very contagious. I also appreciate the help from the staff at the Nano Fabrication Center and the staff from the physics machine shop.

Lastly I wish to thank my family, my mom Meiqin Yan and my dad Zhongwei Guo for supporting me and encouraging me to pursue a life I love.

Feng Guo
University of Minnesota
August, 2011

To mom and dad,

whose constant support and strong faith in their son exactly displayed something called love

Abstract

Electronic noise not only limits the performance of magnetic devices in practical applications but also provides valuable physical insights into these devices. The first part of this thesis discusses how the low frequency noise in magnetic tunnel junctions and giant magnetoresistance devices can be used to understand the fundamental noise sources. Previously, the low frequency noise in these systems has been reported to have an enormously large magnitude when the magnetization switches. This was attributed to magnetic fluctuations. An alternative mechanism of a slow drift in the device resistance is discussed, and we show how it produces noise spectra that are similar to those in previous reports. We conclude that this resistance drift causes a measurement artifact and the low frequency magnetic noise is not present in the measured samples within measurement error. As a second part of the thesis, we discuss a pronounced voltage dependent conductance feature present at nonzero bias in some magnetic tunnel junctions. The presence of this feature depends upon the oxidation condition for creating the barrier, and this effect is found to be interfacial in nature. We describe how the electronic structures and density of states at the barrier interfaces could be responsible for this effect, and possibility of utilizing the conductance measurement to probe the interfacial states.

Table of Contents

List of Figures

Chapter 1:

An Introduction

1.1 Background: giant magnetoresistance (GMR) devices, magnetic tunnel junctions (MTJ) and a snapshot

Giant magnetoresistance (GMR) devices consist of a structure with alternating ferromagnetic and non-magnetic thin film layers. As the name implies, it has a magnetoresistance effect: the resistance depends on the relative magnetization orientations of the adjacent ferromagnetic layers. The total resistance is low (high) when magnetizations are parallel (P) (antiparallel, AP) to each other. The GMR ratio is defined by the resistance difference in P- and AP-state divided by the resistance in P-state, GMR=(R_{AP}-R_P)/R_P. There are two common types of GMR: multilayer GMR which has more than two layers of ferromagnets and tri-layer GMR with two ferromagnetic layers sandwiching a thin non-magnetic spacer. The tri-layer type was primarily fabricated and studied in this study.

Magnetic tunnel junctions (MTJ) are almost identical to tri-layer GMR structures except the spacer is replaced by a thin insulating layer for electrons to tunnel across.

The choice and growth quality of the insulator, typically being AlO_X and MgO, largely determine the device performance. Just as for GMR, the tunneling magnetoresistance (TMR) ratio is defined by $TMR=(R_{AP}-R_P)/R_P$. In general, the TMR ratio is usually much higher than the GMR ratio.

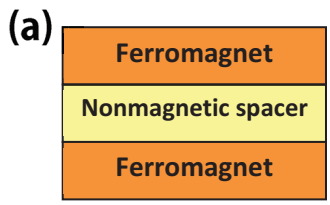

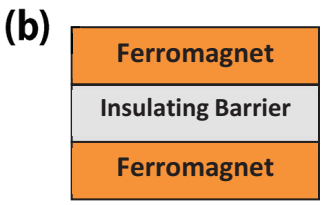

Figure 1.1

Cartoons of (a) a GMR structure and (b) a MTJ structure

The major work of this PhD contains two parts: the noise measurements in MTJs/GMRs (chapter two) and tunneling conductance (chapter three). A very brief introduction for each chapter is described as follows. More detailed background is discussed in the first section of individual chapters.

The noise in the spin-valves is a limiting factor for device performance [1] and our investigation was to determine if the low frequency noise is magnetic in origin. In chapter two, very low frequency noise (much lower than magnon frequency, typically $<10^5$Hz) is discussed. The observation of noise studied as a function of applied magnetic field is first introduced. In magnetic states where the magnetization is reversing, the measurement indicates a $1/f^2$ spectrum whereas at all other applied fields a 1/f spectrum is observed. The $1/f^2$ spectra are found to be an artifact of the magnetic aftereffect. Without the artificial influence of the magnetic aftereffect only 1/f spectra are observed. This is then followed by a discussion of the how much a slow time evolution is required to give rise to this artificial $1/f^2$ spectrum. Finally, as another crucial tool to study spin dependent tunneling process, shot noise was measured in MTJs and the related discussion is attached in Appendix 2.

In chapter three, we discuss an abnormal minimal conductance observed at nonzero voltage in some CoFe/AlO_X/CoFe magnetic tunnel junctions; this pronounced conductance feature occurred for electrons tunneling from the bottom to top electrode. The presence of this conductance feature depends upon the oxidation time for oxidizing the thin Al layer; it is only present for short and moderate oxidation times. Studies on X-ray photoelectron spectroscopy have been done to determine the chemical states of the barrier interfaces and origin of this feature; the conductance feature is observed only when the top CoFe layer is partially oxidized and disappears when the CoFe on both sides of the junction have some oxidation present. A correlation between the asymmetry of the chemical states of the barrier interfaces and the asymmetry of the bias dependent conductance is found. We discuss how the electronic structure and the density of states of CoFe/AlOx bottom interface can be responsible to the differential conductance feature.

1.2 Sample fabrication

All GMR and MTJ samples were fabricated in a UHV deposition chamber. The base pressure is usually about 4×10^{-8} Torr, and the argon pressure during deposition is set to be 3mTorr. The films were grown on SiN (200nm) coated Si wafers using DC/RF magnetron sputtering at ambient temperature. Typical power applied to targets is in the 10-40 Watt range. For these magnetic stacks, a pair of permanent magnets was attached to the sample holder resulting in a growth field of roughly 2kOe. Typical structures of GMRs and MTJs are shown in Fig. 1.2 and detailed stack information and growth and oxidization conditions for each sample can be found in the GMR/MTJ log books in the laboratory.

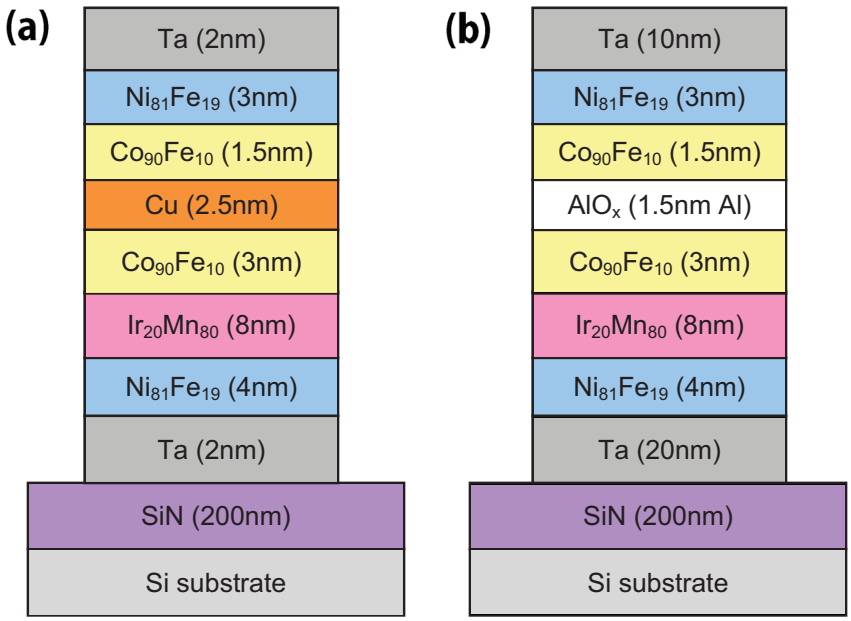

Figure 1.2

Typical stacks of (a) an exchange biased tri-layer GMR device and (b) a bottom biased MTJ structure on silicon nitride coated silicon substrate.

For MTJs, the formation of the tunnel barrier is particularly critical for the TMR ratio. Two methods are used to form the barrier: natural oxidation and target assisted plasma oxidization, both of which are done in-situ without breaking the vacuum. Natural oxidation is done by first depositing 1.5nm thick metallic Al then by transferring the sample to a separate vacuum chamber (Load Lock) sealed with static ultra-pure O_2 gas (pump valve closed). The O_2 pressure for this method is typically around 1Torr and oxidation time is in the 10^3 seconds range. The major problem with the natural oxidization process is that it is difficult for the Al barrier to be thoroughly oxidized since a self-limiting AlO_x layer forms at the surface of the barrier that prevents the arriving oxygen particles to penetrate deep into the barrier (TMR typically <10%). Two-step oxidization is then introduced to overcome this limitation: half of the Al layer is deposited and oxidized and then the second half of the Al is sputtered on top of the first half, and subsequently oxidized. This guarantees some oxygen inside the barrier, and shows slightly improved TMR (10-15%).

A better alternative, used for most tunnel junctions in this thesis, is plasma oxidization. Similar to natural oxidation, a layer of metallic Al is first sputtered on top of the bottom ferromagnetic electrode, and then an Al target gun is lit with a mixture of O_2 (5mT) and Ar (5mT) gases. The oxygen plasma is therefore formed assisted by the Al target (the target is only used for forming plasma rather than deposition as in reactive deposition). In this way, the oxygen particles are ionized and have fairly high kinetic energy. Thus it is easier for oxygen to penetrate into the Al barrier and to bond with Al atoms. Plasma oxidized MTJs turn out to have much higher TMR than those made with natural oxidization. Optimized plasma oxidization can lead to a TMR of up to 40% at room temperature.

Shadow masks were used in the early stage of our MTJ studies [2] to define the junction area which is typically 300x300um^2. Later on a subtractive patterning method with photolithography and ion mill techniques replaced the shadow mask approach for several important reasons. With the new method junction sizes were reduced to the micrometer range (10x10um^2 to 35x35um^2), which made the MTJs more immune to defect and pinholes as compared to larger samples. In other words, smaller samples have higher success rate. Furthermore, multiple samples can be made during a single fabrication cycle: with our current masks, 54 junctions with 6 different areas can be produced from one 1x1 inch substrate (while shadow masks can only make about 2 samples at a time). Also with photolithography, the edges of the junctions are much sharper and better defined, leading to a relatively uniform resistance area (RA) product across the entire substrate. Appendix 1 contains the detailed patterning procedure.

Both the MTJ and GMR samples were usually post annealed *ex-situ* with a field of ~200Oe in the same direction as growth field. The samples were heat treated for one

hour at a temperature of about 250°C. This helps to improve the ferromagnet-anti-ferromagnet coupling and therefore will enhance the coercivity of the pinned layer. Furthermore, a proper heat treatment also improves barrier quality for the MTJs. The thermal energy during the heating tends to make excessive free oxygen diffuse and encourages the oxygen to bond with available aluminum atoms in a more stable configuration, resulting in a more uniform barrier. This is consistent with the fact that an annealed tunnel junction commonly has a more symmetric conductance versus bias voltage curve and a higher TMR ratio. However, over-heating (above 300°C) degrades the TMR due to the excessive interlayer diffusion.

References

[1] Z. Q. Lei, G. J. Li, William F. Egelhoff, Jr., P. T. Lai, and Philip W. T. Pong, IEEE Trans. Magn. 47, 602 (2011)

[2] G. McKusky, *Density of states effects in nickel based magnetic tunnel junctions.* Ph.D. Diss. University of Minnesota, 2009. Dissertations & Theses @ CIC Institutions, ProQuest. Web. 4 Aug. 2011 (Publication Number: AAT 3387288)

Chapter 2:

Low Frequency Noise Measurements

2.1 Background and motivations: in search of magnetic noise

Directly triggered by the discovery of giant magnetoresistance (GMR) [1, 2] and the development of magnetic tunnel junctions (MTJ) [3, 4], the field of spintronics has been undergoing rapid development for the past two decades. On one hand, GMR/MTJ spin valves are a perfect system for spin dependent transport study, offering many interesting problems that have attracted many researchers [5]. On the other hand, the spin valve systems attract tremendous attention from industry due to their immediate impacts on applications such as hard drive read head sensors and other magnetic field sensors. In particular, the noise study in these magnetic systems has been realized as critical for both physics and application reasons. Investigating the noise provides a unique approach to study various physical processes that regular transport measurements do not have access to; at the same time, understanding the noise also immediately benefits the noise reduction and therefore the signal-noise-ratio enhancement especially for disk drive read heads and magnetic field sensors.

As a brief introduction to the noise spectrum, there are three major noise components: 1/f noise, shot noise and Johnson noise. At the lowest frequencies, typically 10-10,000Hz for GMR/MTJs, the power spectral density (PSD) scales with frequency according to a power law with the power exponent commonly close to negative one. Thus this low frequency spectrum is called 1/f noise. It is worth noting that the 1/f noise is universally observed in an extremely wide range of systems. The mechanism for 1/f noise, on the contrary, is not well-known despite its long history and is not necessarily universal [6]. Moving to higher frequencies, 1/f noise is replaced by Johnson and shot noises. Both Johnson and shot noises are frequency independent and therefore together fall into the category of white noise. Johnson noise, with an alternative name of thermal noise, is due to the thermal fluctuation of charge carriers. It is proportional to the temperature and device resistance as a result of the fluctuation-dissipation theorem. Though it could be a very small signal, Johnson noise persistently occurs in any resistive system at nonzero temperature. Shot noise, different from Johnson noise, results from the random injection of the carriers with a discrete charge (usually one electron charge *e*). In a system where the randomness is washed out (complete anti-correlation), the shot noise vanishes. For GMR devices, shot noise is not expected unless the sample size is comparable to the electron coherence length at very low temperatures [7]. MTJs, however, are expected to have some shot noise since the tunneling events are random. In fact, tunnel junctions are often used to calibrate shot noise levels in many experiments.

1/f noise is primarily discussed in this chapter (shot noise in Appendix 2). In the case of MTJs there have been a number of studies that focus on the noise [8-15]. A significant increase in the low frequency noise (i.e. by a factor of 10 to 100) when a magnetic layer is reversing has been reported [8-14] and was attributed to magnetic fluctuations. A large deviation in the spectral exponent, α, as in $1/f^{\alpha}$, from the

common value of 1 to about 2 was reported in two papers [14, 15], and was also attributed to being magnetic in origin. In order to better understand these previous results, we focused on the origin of the purported low frequency noise and its correlation with the magnetic state as an extension of our previous work [16].

In this chapter, I will first discuss the experiment setup, measurements of the noise, and its results associated with the time dependence of the MTJ/GMR device resistances. The time evolution experiments in section 2.4 show the drifting of the device resistance after a field value was reached and then kept constant. This clearly indicates the presence of a magnetic aftereffect in the devices when a magnetic layer is switching. A study of the time dependence of the noise spectra (repeated measurements of the noise) after a target magnetic field was reached directly shows how the magnetic aftereffect can give rise to a measured increase in the low frequency noise and can increase the frequency dependence of this noise from 1/f to $1/f^2$ depending upon the amount of magnetic aftereffect present. Therefore the magnetic aftereffect must be considered in noise measurements on magnetic devices. Our conclusion from this study is that the previously reported increase in the magnitude of low frequency noise and the increase in α to values larger than 1 can arise from a mixing of the 1/f noise, which is always present, and a slow time relaxation of the magnetic state commonly referred to as the magnetic aftereffect (or magnetic viscosity). When accounting for the magnetic aftereffect we only find 1/f noise present and a similar magnitude of the low frequency noise for all magnetic states. I also describe two experiments attempting to determine any magnetic contributions to the low frequency noise. One is an investigation of the noise in large magnetic fields and the other is measurements of the noise as a function of the angle between the magnetizations. Finally, I discuss a calculation showing quantitatively how time evolution distorts intrinsic 1/f noise spectrum.

2.2 Experimental setup

For the noise measurements the current source consists of a 1.5V C-cell battery in series with a current limiting 200kΩ resistor; the sample voltages were amplified (typical gain of 10^3) with a SR560 amplifier used in battery mode before the power spectral densities, PSD or S_V, were measured with a HP34560A spectrum analyzer (Fig. 2.1). The sample and electromagnet were enclosed in a shielding box made of 0.8mm thick aluminum sheet. The shielding box was connected to the low potential terminal of the sample and was grounded. This setup has been found to be immune to electromagnetic radiation from the environment including the 60Hz power line noise and its harmonics. A four-terminal connection was used for the transport; all the data we presented here were taken at ambient temperature. The noise data was averaged over multiple measurements (i.e. 25) and for the noise data shown the preamp gain has been removed.

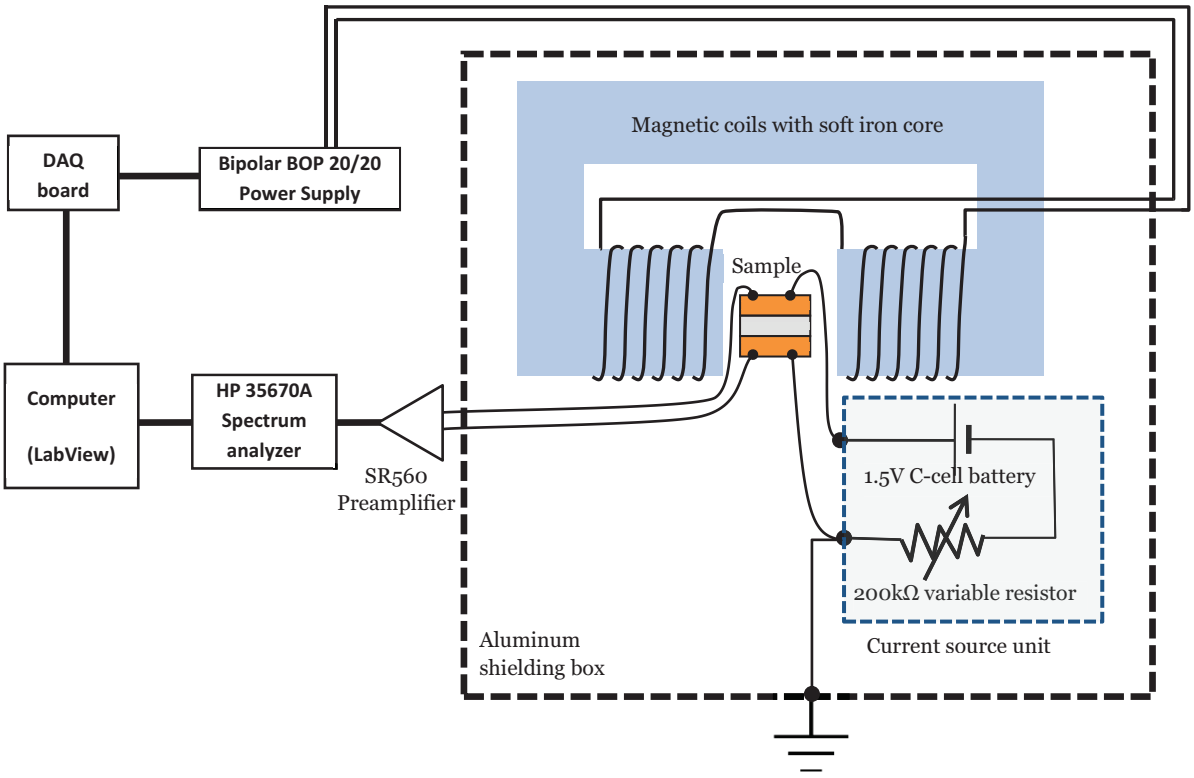

Figure 2.1

Schematic set-up for noise measurements

2.3 Magnetic state dependence of 1/f and $1/f^2$ noise spectra

Figure 2.2a shows a typical noise spectrum of a MTJ with parallel magnetizations (similar for antiparallel state) with 80mV applied bias voltage. Note this is a log-log plot. As shown at low frequencies, below 1 kHz for example, the noise scales as 1/f as indicated by the solid green line with a slope of -1 beneath the low frequency part of

the spectrum. At higher frequencies the spectrum becomes frequency independent consisting of a combination of Johnson noise and shot noise; the dashed line is the calculated white noise (Johnson noise plus shot noise) based on the junction resistance. The same figure shows the noise from a metal film resistor without an applied voltage having a resistance comparable to that of the MTJ sample. Clearly the MTJ 1/f noise is larger than the background noise but the question is if this is magnetic noise or noise from other sources such as the oxide tunnel barrier. For now we simply state we can find no evidence this 1/f noise is magnetic in origin and will return to this statement later in the chapter.

In both the parallel (P) and antiparallel (AP) magnetic states the spectra of the MTJ and GMR devices all exhibit similar behaviors. The main difference between the MTJ and GMR devices is the white noise in the GMR devices is exclusively from the thermal noise due to the large size (millimeters) of the device. The magnitude of the 1/f noise is found to be proportional to the applied voltage squared, for both MTJs and GMR samples (Fig.2.2b). For all the noise spectra and resistance measurements shown in the following, a constant current value was applied to the sample through the entire experiment. The corresponding applied voltage was typically in a range of 10-100mV so that the 1/f noise from the sample was much larger than the background signals (background is the spectrum measured from a metal film resistor with a similar resistance to the sample's such as the red spectrum in Fig. 2.2a). Also, the voltage drop across the sample was still much smaller than the total battery voltage. (Note that the applied voltage is varied via a variable resistor. The measured noise is correct only when the variable resistance is much bigger than the sample resistance. For example, no noise will be measured if the variable resistor is short assuming a perfectly noiseless battery.)

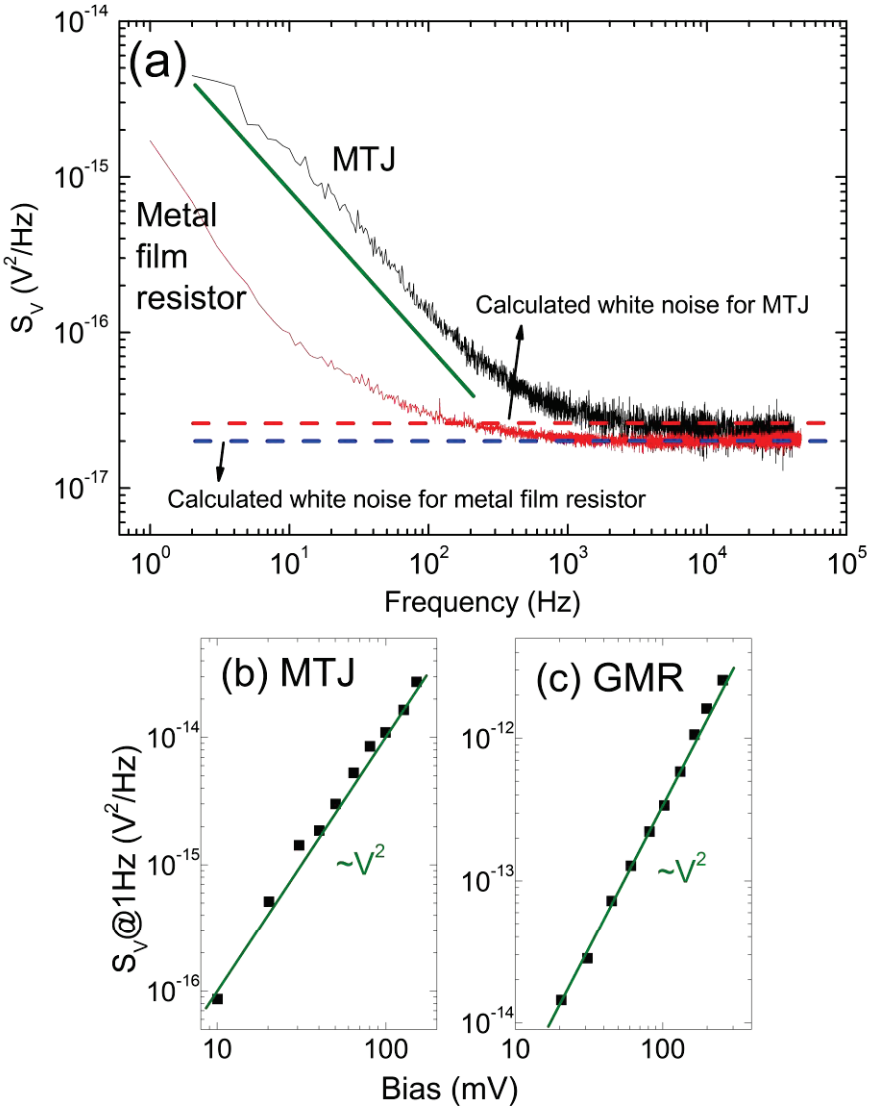

Figure 2.2

(a) Typical noise spectra for a MTJ (black) with junction resistance of about 270Ω in the P-state with 80mV applied voltage and a 274 Ω metal film resistor (red). The green solid line beneath the MTJ spectrum has a slope of -1, indicating the *1/f* nature of the spectrum; the upper horizontal line (red dash) is the calculated noise level including the thermal and shot noise; the lower line (blue dash) shows the calculated thermal noise for the metal film resistor. Figures (b) and (c) show the bias dependence of the 1Hz S_V for a MTJ and a GMR sample, respectively, measured in P-state. The solid lines in (b) and (c) indicate a V^2 dependence.

For both MTJs and GMR samples, the magnetoresistance and the magnetic field dependence of the noise spectra were measured. 20 MTJs and 10 GMR samples were used for the study, and they all yielded similar results. Representative examples of magnetoresistance measurements for a MTJ and a GMR device are plotted in Figs. 2.3a and 2.3c respectively; the device resistance state infers the magnetic state; for example the magnetizations of MTJ is in P configuration of low resistance state in points A and E and is close to AP configuration in point C due to the higher resistance value; and points B and D indicate the transition states – in which soft layer and hard layer, respectively, are undergoing reversal. The situation is similar for the GMR in Fig. 2.3c.

Noise spectra were measured for various magnetic states, and 1/f noise was observed to dominate below about 2×10^3Hz. Figures 2.3b and 2.3d show the measured noise in different magnetization configurations. A 1/f spectrum was observed in both the P or the AP states (i.e., points A, C, F, and H) as indicated by the green solid lines with a slope of -1; furthermore there was no significant difference in the magnitude of the 1/f noise for either the P or the AP sates; however, in the transition states (points B, D, G, and I) completely different noise behaviors were measured; these spectra have a slope of about -2 as shown by the red lines, and thus are $1/f^2$ spectra rather than 1/f as in the P and AP states. In addition to the spectral exponent, the noise magnitude of the $1/f^2$ spectra is also larger than that of 1/f noise in the P and AP states by a factor of over 100. The increase in both noise level and spectral exponent during the magnetization switching is a universal behavior among all the measured MTJs and GMR samples.

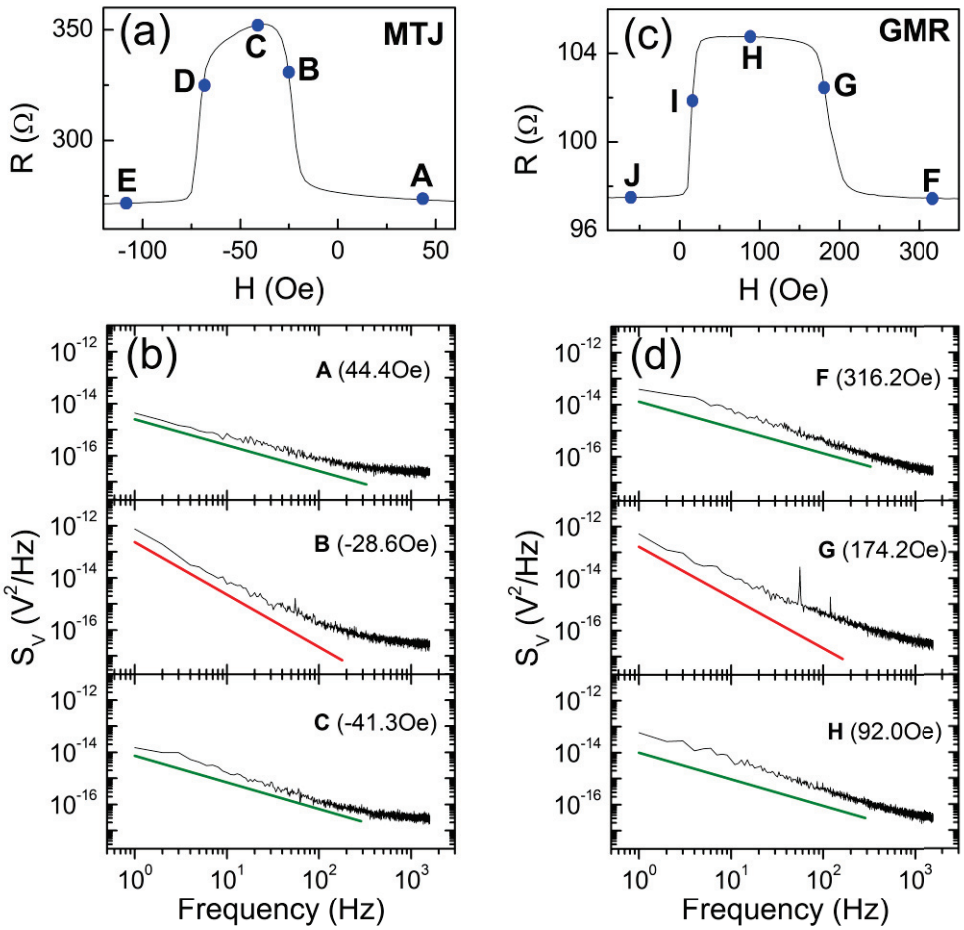

Figure 2.3

The plots (a) and (c) are the dc resistance of the MTJ and GMR samples respectively with a magnetic field swept from positive to negative values. When measuring the spectra, 50mV and 160mV bias voltages are applied to the MTJ and GMR samples respectively. The three plots in (b) are PSDs of the MTJ sample taken at the points A, B, and C marked in the resistance curve. The PSD taken at the point marked E is similar to that taken at point A, and B is similar to D. In plots labeled A and C in (b) the solid lines are 1/f and in B it is$1/f^2$. Shown in (d) are the same noise measurements for the GMR sample and similar features are observed; the spectra in the parallel states, points F and J, and antiparallel state, point H, have 1/f noise. During the magnetization reversal, such as points G and I, the noise scales as $1/f^2$ as illustrated by the line under the data in the spectrum labeled G.

In order to illustrate the magnetic state dependent noise data in detail, we characterized the spectra with two parameters – the PSD magnitude at 1Hz and the exponent α obtained by fitting the spectra with $1/f^{\alpha}$. These two quantities are plotted as functions of the magnetic field in Fig. 2.4 for the same MTJ and GMR samples as in Fig. 2.3. As one can see in Fig. 2.4, for both the MTJ and the GMR sample the noise behaves similarly in the P and AP states as is consistent with complete spectrum measurements in Fig. 2.3. Since the applied current is relatively small (10μA-1mA), the voltage difference in P and AP state is not large enough to resolve the noise difference these two states. (The noise levels for the P and the AP state will separate for higher bias). Also the spectral exponent α in both the P and AP states is close to the value of 1. Like the previous noise studies [8-15], the unexpected noise behaviors were observed in the transition regions when either the free layer or hard/pinned layer is in the process of switching. As can be seen, in these regions the noise can be over 1000 times larger for the MTJ sample and approximately 100 times larger for the GMR sample compared to the noise in either the P or the AP states. In addition to the increase in the noise level, the exponent α increases from the usual value of 1 to values as large as 2.

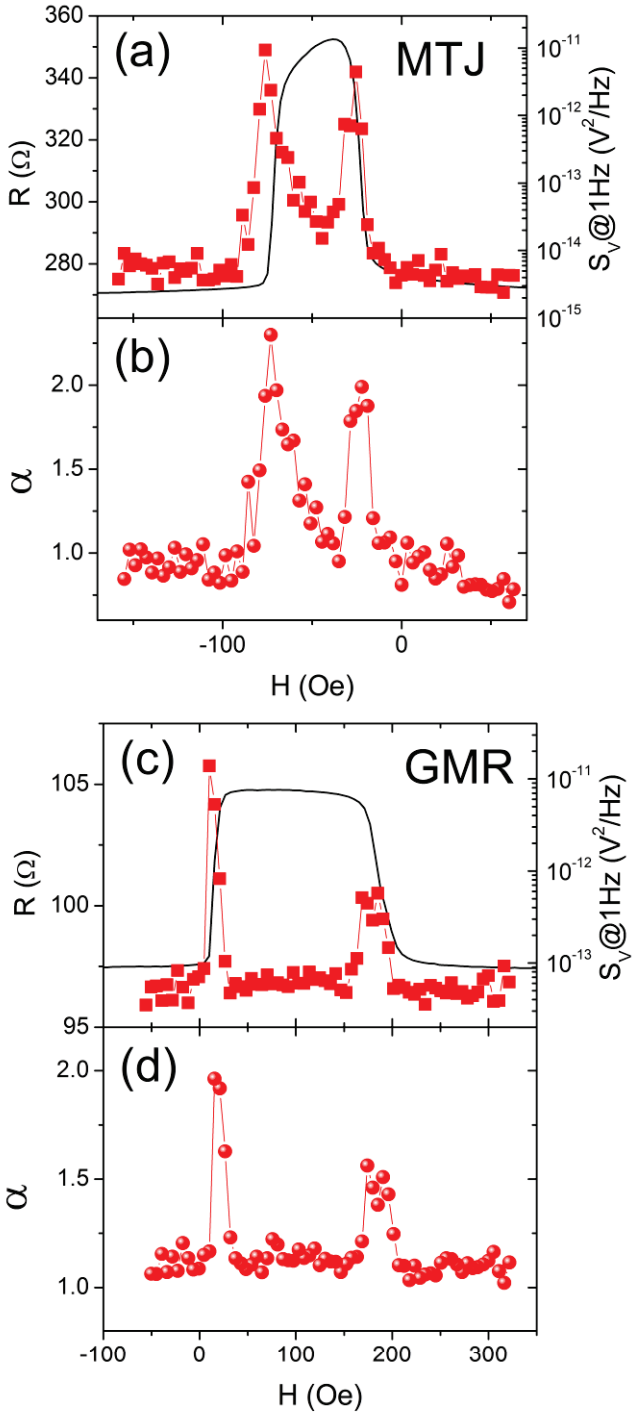

Figure 2.4

Two parameters, the PSD at 1Hz and the spectral exponent α, used to characterize the measured noise spectra are shown for a MTJ and a GMR device. The MTJ PSD noise magnitude (squares) as a function of the magnetic field is shown in (a); and α fitted from the low frequency part of the spectrum is plotted in (b). The GMR noise magnitude (squares) is in (c) and α is in (d).

2.4 Time domain signals – magnetic aftereffect

To understand the deviation of the noise spectra in the transition regions from those in the P and the AP states, we investigated the voltage signals in the time domain at various magnetic fields before they were Fourier transformed into power spectra. Constant currents were applied to the MTJs and GMR devices for this measurement. The procedure began with the application of a large positive magnetic field to saturate the magnetizations so that the sample started in a parallel magnetic configuration. The magnetic field was then swept in the negative direction until the desired field value was reached and then the measurements of the time dependent resistance (or voltage) were started. The usual time for data collection was about 100 seconds [17].

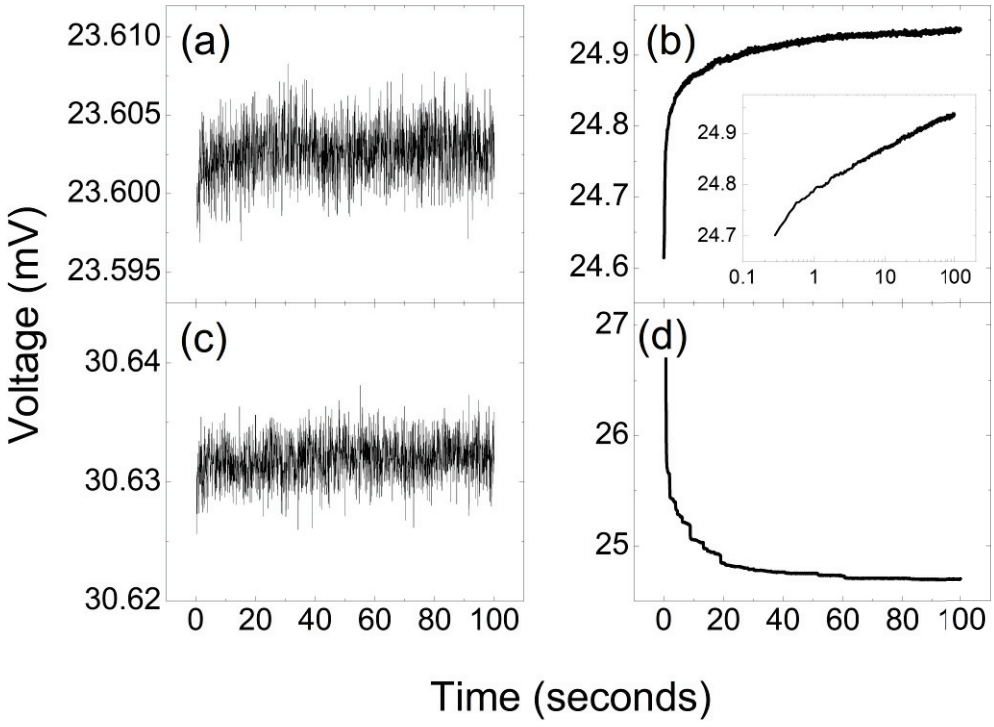

Figure 2.5

Time dependence of the voltage of a MTJ starting when a target magnetic field is reached: the data in (a) were taken in the P state such as point A in Fig. 2.3, those in (b) were taken in the P to AP region (soft layer switch) such as point B in Fig. 2.3. The data in (c) correspond to the MTJ in an AP state such as point C in Fig. 2.3, and the data in (d) correspond to the AP to P region (hard layer switch) similar to point D in Fig. 2.3. Note that (b) and (d) have larger vertical scales. The inset in (b) is the same as the P to AP data plotted using a logarithmic scale for the time as is usually done for the magnetic aftereffect.

As the results of these time domain measurements were qualitatively the same for all the samples of both the MTJ and GMR device structures we show a single illustrative example in Figure 2.5 for a MTJ. In both the P and the AP states as seen in Figs. 2.5a and 2.5c respectively, the voltage is essentially time independent. When Fourier

transformed to determine the power spectral densities, the voltage signals in both the P and AP states give 1/f noises as one would expecte. At the fields corresponding to the transition regions (Figs. 2.5b and 2.5d), however, we observed significant time dependent drift in addition to the noise beyond the transition regions. This large monotonic time dependence is attributed to the magnetic aftereffect or magnetic viscosity [18, 19]. Typically the magnetic aftereffect has a quasilogarithmic time dependent magnetization which we show in the inset of Fig. 2.5b where a plot of the logarithmic time dependence of the voltage, taken as a measure of the magnetization, is presented. One should note the variation of the voltage within the 100 second measurement time due to the magnetic aftereffect is significantly larger than the voltage fluctuations in either the P or the AP state. The Fourier transform of a logarithmic signal gives $1/f^2$ behavior in the noise power. Thus for these time signals with a significant time dependent voltage evolution, doing an apparent noise calculation will result in a $1/f^2$ like spectrum and enormous noise levels; the noise magnitude is from the large logarithmic dependence of the voltage drift (magnetic aftereffect). We will discuss more on this later in this chapter.

2.5 Influence of magnetic aftereffect on measured noise

What we show next is how the presence of a magnetic aftereffect explains the observed low frequency noise increase and the deviations from 1/f behavior, i.e., they are both artifacts of the magnetic aftereffect and not a measure of magnetic noise. One way to accomplish this is to look at the time evolution of spectra at the fields in transition regions; another way is to compute the noise of the mixture of original 1/f signals and extra “noise” due to the magnetic aftereffect.

We now describe the first approach – measuring the noise spectra repeatedly over a long time period. As one expects, the voltage change per unit time associated with the magnetic aftereffect becomes smaller with each noise measurement and it will eventually become insignificant compared to the intrinsic 1/f signals, thus its contribution to the measured spectra reduces with time. In essence, measuring the spectrum repeatedly at a specific field value has the same effect as reducing the magnetic aftereffect. The procedure we followed for this study is similar to the time dependent voltage measurements described above. First the magnetizations were saturated with a large positive magnetic field. Then the field was swept in the negative direction until the switching region of one of the magnetic layers was reached (points D and B in Fig. 2.3a and points I and G in Fig. 2.3c). Upon reaching a field value in the transition region, the magnetic field was held constant while the spectrum was measured repeatedly over a period of time. After this process a number of spectra were taken at various times at the target magnetic field. In this way the time evolution of the spectra was obtained. Examples of the results of these studies are presented in Figs. 2.6a and 2.6b for a MTJ and a GMR sample respectively as the soft layer is switching. The PSD at 1Hz and α were obtained from each measured spectrum and the time evolution of the two is plotted. As shown the spectra for both devices begin with a large low frequency noise level exemplified by the 1 Hz noise magnitude and a large value of α like the noise data in the transition regions in Figs. 2.3 and 2.4. Over 400 seconds, as the contribution from the aftereffect was diminishing, the PSD at 1Hz gradually decayed to a value that was consistent with the noise level in the P and AP states and simultaneously the value of α decreased from 2 to 1. These measurements clearly indicate the logarithmic variation of the device voltage alters the measured spectra.

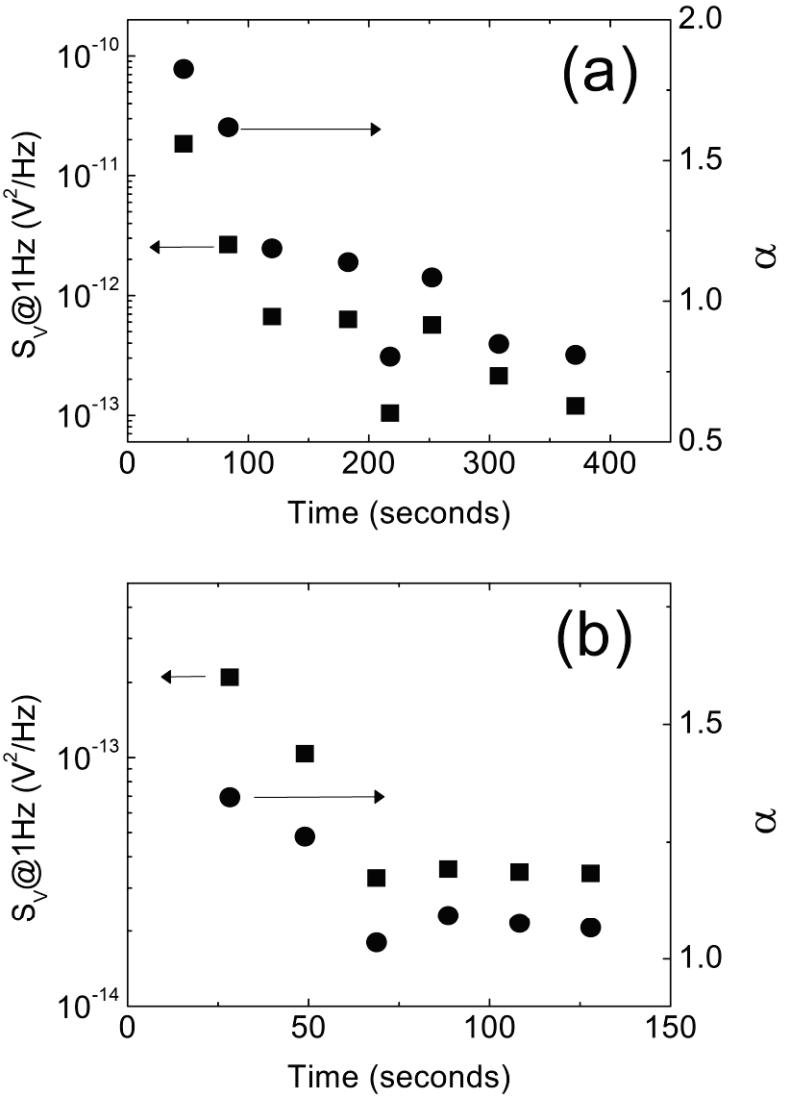

Figure 2.6

The fitted value of the exponent α (circles) and the magnitude of the PSD at 1Hz (squares) of a MTJ (a) and a GMR device (b) as functions of time at a constant field in the P to AP transition region of each.

As a second approach, we now show for an analytical function slowly changing the voltage across the device (no Barkhausen), both the magnitude of the low frequency

noise level and the $1/f^2$ spectrum in the transition regions are an artifact. In more detail, we generated a time dependent signal having a pure 1/f spectrum with the 1Hz component set to a value of $3\times10^{-15}V^2/Hz$ which is comparable to the measured noise level for our MTJ devices. This 1/f noise was then added to a function to replicate the magnetic aftereffect which was a logarithmic function of the form $A_{AE}\,\mathrm{Log}(t+0.1)$ with the magnitude of the prefactor A_{AE} determining the amount of magnetic aftereffect present. In other words, if A_{AE} =0 then there is no magnetic aftereffect just like the P and the AP states and any nonzero values of A_{AE} indicate the presence of some magnetic aftereffect. The PSDs of these simulated time signals were determined for various values of A_{AE}, with the results of the magnitude of both the PSD at 1Hz and α as functions of A_{AE} plotted in Fig. 2.7a. As one can see from these figures as A_{AE} is increased, equivalent to increasing the magnetic aftereffect present during a measurement, the spectra evolve from 1/f to approximately $1/f^2$ while the magnitude of the 1 Hz noise also increases by a factor of about 1000 for the values of A_{AE} used; the saturation of α to a value close to 2 can be shown analytically as described in the next paragraph. A parametric plot of α and the 1Hz PSD magnitude illustrating their correlation as A_{AE} increases is shown in Fig. 2.7b. To compare this with actual noise data, Figs. 2.7c and 2.7d show the correlation between α and the 1 Hz component of the spectra presented in Fig. 2.4 for the MTJ and the GMR device respectively.

Alternatively, one can also show how a logarithmic function alters the measured spectra in a more analytical fashion, i.e., calculating the PSD of the logarithmic function, $A_{AE}\,\mathrm{Log}(t+t_0)$. This is most easily accomplished by taking the Laplace transform with time domain variable *t* being transformed to a complex variable *a + iw* and then taking the limit as *a* goes to zero. When this is done, one finds PSD's of the form $1/f^{\alpha}$ with α approaching to 2 for t_0 on the order of 0.1 sec and the

magnitude of the PSD determined by A_{AE}. This analytical approach also explains the saturation of $\alpha \approx 2$ seen in Fig. 2.7b. (i.e. within 1-1000Hz frequency window: for t_0=0.1s, α=1.85 and for t_0>10s, α=2.00).

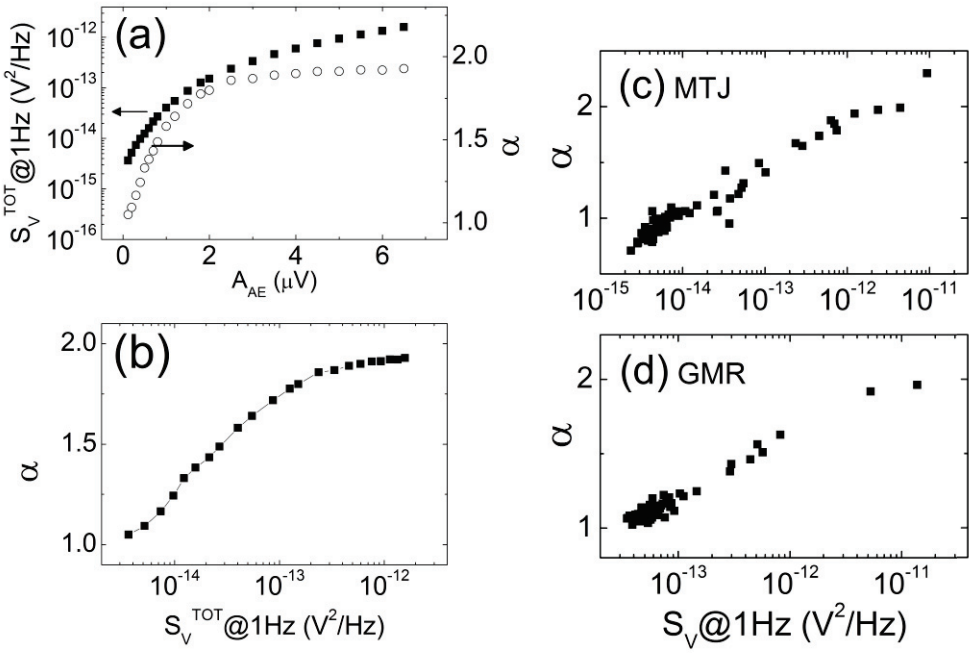

Figure 2.7

(a) For the spectra calculated from the simulated total time signals, the value of the 1Hz PSD and the value of α are plotted as functions of A_{AE}, which determines the magnitude of the magnetic aftereffect; (b) shows the correlation between α and PSD at 1Hz; (d) and (e) are the data from Fig. 3 for the MTJ and GMR samples respectively as a comparison.

The next obvious question to ask is how large a change in voltage across a device during a measurement period due to the logarithmic time dependence of the magnetic aftereffect would be necessary to distort the measurements. This is rather

difficult to answer in general but the above simulation offers one quantitative measure of this effect. Consider the situation where the magnetic aftereffect causes a resistance drift. We define a quantity, δV, to be the voltage change over the measurement period (1 second for the data shown in figure 2.8). To understand how this δV affects the measurements, we calculated the PSD one would obtain as a function of δV. This calculation included only the logarithmic function without any added 1/f component. In figure 2.8a we show a plot of the magnitude of the PSD at 1 Hz, which we call S_V^{Log}, as a function of δV. This clearly shows the remarkable sensitivity of noise measurements to the presence of any magnetic aftereffect. The inset in figure 2.8a shows the PSDs calculated for several values of δV; the slope of the PSDs, α, is about 2.

Since the PSD associated with the magnetic aftereffect and the actual noise in a device are uncorrelated, their combined effect on the noise power would be additive. Thus a determination for how large a magnetic aftereffect voltage change during a measurement time, δV, is best illustrated by considering the ratio of the total PSD value at 1 Hz from both the magnetic aftereffect and the actual device noise to the value of the PSD at 1 Hz in a typical device without any measureable aftereffect present. This ratio is plotted in figure 2.8b as a function of both δV (lower X-axis) and as a percentage of the device bias voltage (upper X-axis) which is about 50mV in this case. As can be seen in this figure, extreme care must be taken in assuring the device being measured is close to equilibrium as an even small magnetic aftereffect voltage can drastically alter the measurement results. For example, a small voltage drift in 1 second with $\delta V=6\times10^{-6}\ V_{bias}$ already doubles the total PSD with respect to the original PSD; and a voltage drift of only $\delta V=1.6\times10^{-5}V_{bias}$ will spuriously change the measured PSD by a fact of 10. In Fig. 2.9, three examples with different δV values are shown to

further illustrate that even small voltage drifts that are barely noticeable in time measurements can significantly alter the noise power measurements.

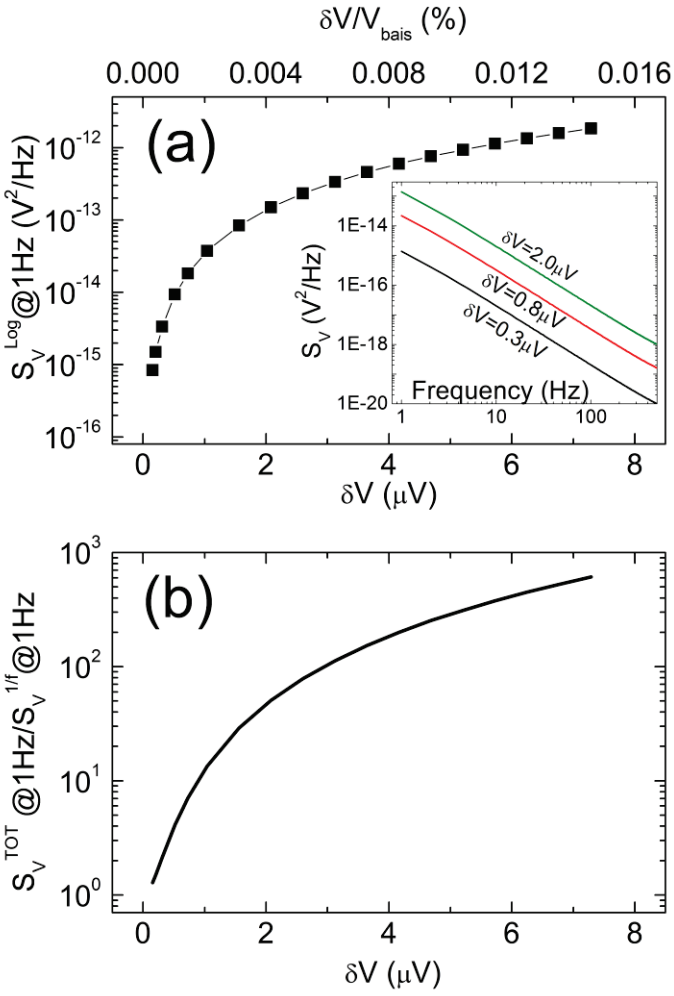

Figure 2.8

(a) The 1Hz component of the PSD calculated for a pure logarithmic function as a function of δV, where δV is the change of the voltage during the measurement time (taken as 1 sec.); the top x-axis shows δV as the percentage of a typical dc bias voltage of 50mV. In the inset is plotted three PSDs of the pure logarithmic function with different values of δV. In (b) is plotted the δV the ratio of the value of the 1Hz component of the PSDs with both the 1/f signal and the logarithmic function included to the value of the 1 Hz component of the PSD for a typical MTJ which is taken as $3\times10^{-15}V^2/Hz$.

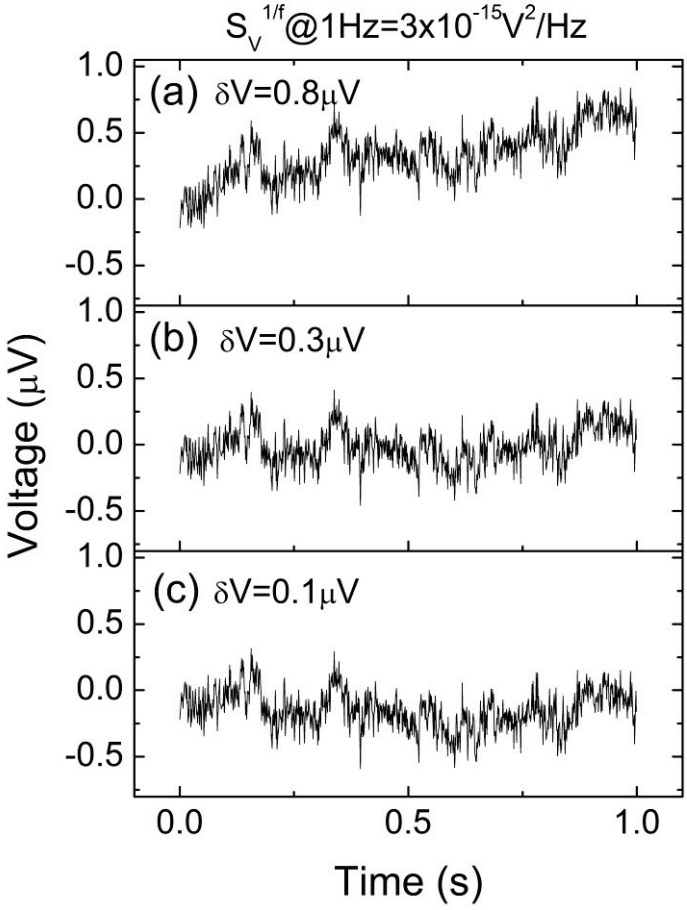

Figure 2.9

Simulated time dependent signals with mixture of 1/f signal (S_V@1Hz=3×10^{-15} V^2/Hz) and a logarithmic function with voltage change δV. Three different values of δV are selected as examples to illustrate how a small voltage drift will give rise to the measurement artifact: (a) δV=0.8, $S_V^{TOT}/S_V^{1/f}$=9.0, α=1.48; (b) δV=0.3, $S_V^{TOT}/S_V^{1/f}$=2.5, α=1.16; (c) δV=0.1, $S_V^{TOT}/S_V^{1/f}$=1.2, α=1.05.

So far, we have explained that the origin of the unexpected low frequency noise in transition regions is purely from the mixture of the device noise and the signal drift due to the magnetic aftereffect. But this raises a separate question. Is there any detectable 1/f or low frequency noise for our MTJ or GMR devices that is clearly

associated with the magnetism as claimed in previous reports? In the next section, we present two experiments which attempt to answer this question.

2.6 Additional experiments

To extend the search for magnetic low frequency noise, two experiments were designed for this part of the study. In the first experiment, a variable magnetic field was applied in-plane to a MTJ with the magnetizations parallel to the field direction. The field was varied from a relatively low value up to 2×10^4 Oe without changing the directions so that the MTJ stayed in the P-state. At a number of fixed magnetic fields, the MTJ voltage and the noise spectrum were recorded. The results of this are shown in Fig. 2.10 where in Fig. 2.10a the MTJ voltage (proportional to the resistance with constant current) is shown and the noise magnitude at 1 Hz is shown in Fig. 2.10b. The 2% drop in voltage indicates that the increasing field forces the magnetizations to be better aligned. However there is no measurable change in the 1 Hz PSD. Although there is no apparent change in the low frequency noise in this measurement, this null result merely sets an upper limit of possible magnetic 1/f noise.

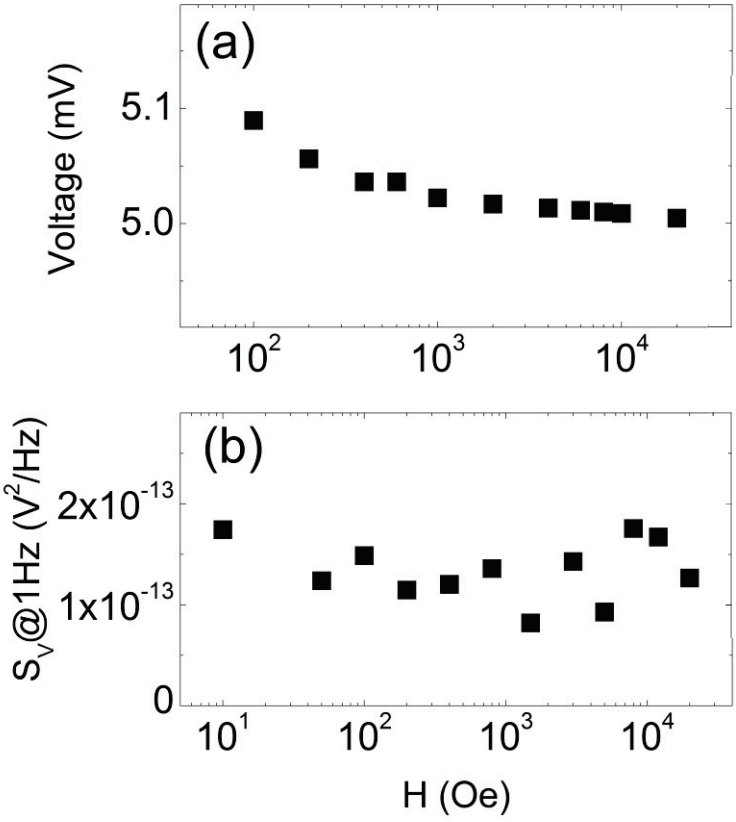

Figure 2.10

(a) Voltage of a MTJ versus magnetic field for a constant applied current; (b) the 1Hz value of the measured PSD as a function of magnetic field.

The second investigation consisted of measuring the noise spectrum as a function of angle between the two magnetizations in a GMR device. An applied magnetic field of 100 Oe was chosen so that it is was well below the switching field of the pinned layer but higher than the switching field of the free layer. By rotating the magnetic field in the plane of the sample only the free layer followed the applied field thereby changing the angle between the magnetizations. The resistance of the GMR device and the noise spectrum were measured as functions of the angle between the magnetizations. The results are shown in Fig. 2.11 where the angular dependence of the device resistance (Fig. 2.11a) and the magnitude of the 1 Hz noise (Fig. 2.11b) are plotted. The resistance versus angle data are consistent with the angular dependence

expected for a GMR device [20] with the P state (0 or 360 degrees) having a low resistance and the AP state (180 degrees) having the highest resistance. The noise spectrum was also measured at various angles and was averaged over 100 measurements. The 1Hz component of the PSD as a function of angle is shown in Fig. 2.11b and no significant angular dependence of noise within the measurement error is observed in the data. Again, although we do not observe any noise in our measured samples which we can attribute to magnetic fluctuations this null result also only sets an upper limit for the magnetic noise.

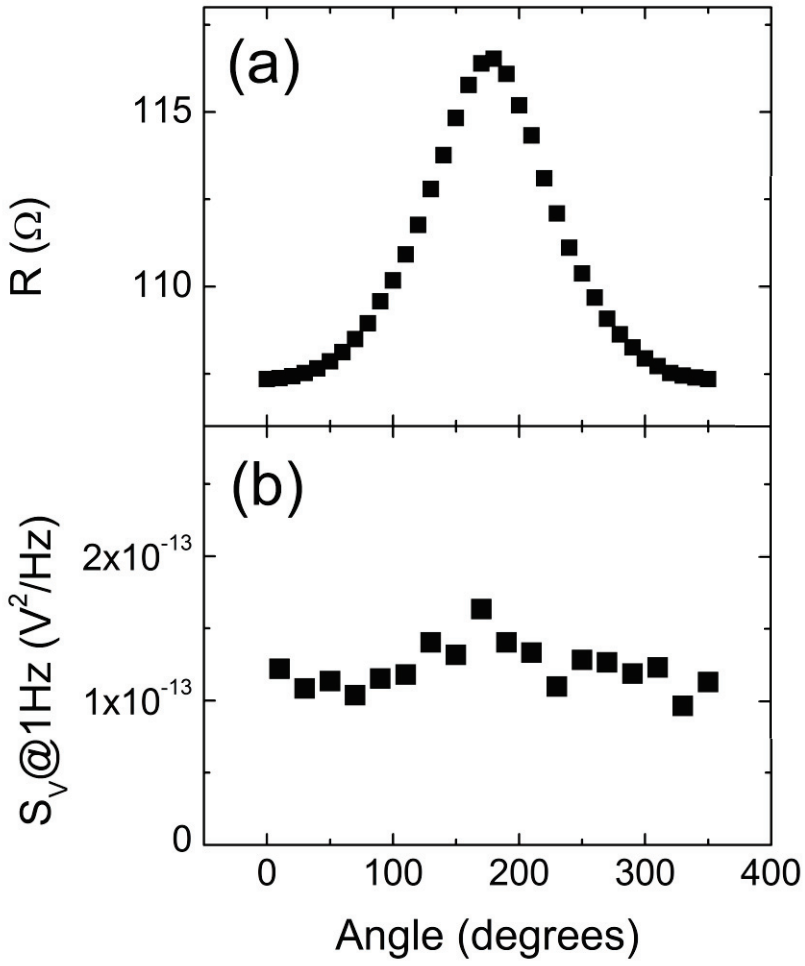

Figure 2.11

(a) The GMR resistance as a function of the angle between the magnetizations in the two layers; (b) the angular dependence of the PSD at 1 Hz.

As a brief summary, our observations of the noise in MTJs and GMR devices in the P and the AP states the spectrum is always 1/f, and the noise levels in these two states, after removing the effect of different voltages, are the same. In the magnetic transition regions where the value of dR/dH was large (P to AP and AP to P transitions) the apparent noise measurements indicated noise spectra of $1/f^{\alpha}$ form with α between 1 and 2 and a related increase in the magnitude of low frequency noise. Further investigation in the transition regions show that time dependence of

the device voltages typically scale as the logarithm of the measurement time. This is related to the time evolution of the magnetic state commonly referred to as the magnetic aftereffect or magnetic viscosity. A causal relationship between the time evolution caused by the aftereffect and both the magnitude of the measured low frequency noise and the apparent noise spectrum exponent was determined in two ways.

The first consisted of measuring the time dependence of the spectrum in transition regions. We found the measured spectrum started as a $1/f^2$ spectrum and then evolved to that of 1/f noise while the 1Hz noise diminished to its normal level (P and AP states) in this relaxation process. The second method calculated the PSD of the sum of a 1/f signal and a logarithmic time dependent function. We found as the amplitude of the logarithmic prefactor increased, consistent with the magnetic transition states, the apparent spectrum evolved to the $1/f^2$ type and there was an associated increase in the low frequency noise level. We also pointed out that this is consistent with the analytically determined PSD for a logarithmic function of time.

These two independent methods directly support our conclusions that the magnetic aftereffect is responsible for the observations of increased noise in the transition regions described in a number of reports [8-14] and the increase in the spectral exponent of the noise from 1 to 2 in other reports [14, 15]. For all of the samples we studied, after removing the artifact resulting from time dependent signals, the low frequency noise spectrum is independent of magnetic state within our measurement error.

In order to continue searching for the possible magnetic 1/f noise, we propose some experiments to achieve this. Based on the fluctuation-dissipation theorem, the possible magnetic 1/f noise is predicted to be inversely proportional to the volume of

the magnetic layer [21]. As the sample size gets smaller (i.e. magnetic dots) the magnetic fluctuation might become more significant (the smallest devices studied in this thesis are $10\times10\mu m^2$ which could be still too big to observe the possible magnetic noise). Utilizing the magnetoresistance effects such as the anisotropic magnetoresistance, one is able to detect the possible magnetic noise by measuring the resistance noise. The volume dependence of the magnetic noise can be verified by varying the size (or thickness) of the magnetic systems. The temperature dependence will answer the question if the magnetic 1/f noise is thermally activated. The magnetic noise is also claimed to be dependent on the saturation magnetization [21], which can be studied by varying the magnetic material. Also, the field dependence will tell one how the noise is related to the magnetization fluctuations (magnetization switching between metastable states), which can be suppressed by applying a large magnetic field.

References

[1] M. N. Baibich, J. M. Broto, A. Fert, F. Nguyen Van Dau, F. Petroff, P. Etienne, G. Creuzet, A. Friederich, and J. Chazelas, Phys. Rev. Lett. 61, 2472 (1988)

[2] G. Binasch, P. Grunberg, F. Saurenbach, and W. Zinn, Phys. Rev. B 39, 4828 (1989)

[3] M. Julliere, Phys. Lett. 54 (1975) 225

[4] J. S. Moodera, L. R. Kinder, T. M. Wong, and R. Meservey, Phys. Rev. Lett. 74, 3273, (1995).

[5] E. Y. Tsymbal, O. N. Mryasov, and P. R. LeChair, J. Phys: Condens. Matter 15 (2003) R109-R142; J. S. Moodera and G. Mathon, J. Magn. Magn. Mater. 200 (1999) 248; J. S. Moodera, J. Nassar and G. Mathon, Annu. Rev. Mater. Sci. 1999. 29: 381-432; S. S. P. Parkin, Annu. Rev. Mater. Sci. 1995, 25: 357; E.Y.Tsymbal and D.G.Pettifor, Solid State Physics, 56, 113 (2001)

[6] M.B. Weissman, Review of Modern Physics, 60 (1988) 537

[7] C. Dekker, A.J. Scholten, F. Liefrink, R. Eppenga, H. van Houten, and C.T. Foxon, Phys. Rev. Lett. 66, 2148 (1991); A.H. Steinbach, J.M. Martinis, and M.H. Devoret, Phys. Rev. Lett. 76, 3806 (1996).

[8] L. Jiang, E. R. Nowak, P. E. Scott, J. Johnson, J. M. Slaughter, J. J. Sun, and R. W. Dave, Phys. Rev. B. 69, 054407 (2004).

[9] C. Ren, X. Liu, B. D. Schrag, and G. Xiao, Phys. Rev. B. 69, 104405 (2004).

[10] S. Ingvarsson, G. Xiao, S. S. P. Parkin, W. J. Gallagher, G. Grinstein, and R. H. Koch, Phys. Rev. Lett. 85, 3289 (2000).

[11] D. Mazumdar, X. Liu, B. D. Schrag, M. Carter, W. Shen, and G. Xiao, Appl. Phys. Lett. 91, 033507 (2007).

[12] D. Mazumdar, X. Liu, B. D. Schrag, W. Shen, M. Carter and G. Xiao, J. Appl. Phys. 101, 09B502 (2007).

[13] D. Mazumdar, W. Shen, X. Liu, B. D. Schrag, M. Carter and G. Xiao, J. Appl. Phys. 103, 113911 (2008).

[14] A. F. Md Nor, T. Kato, S. J. Ahn, T. Daibou, K. Ono, M. Oogane, Y. Ando, and T. Miyazaki, J. Appl. Phys. 99, 08T306 (2006).

[15] R. Guerrero, F. G. Aliev, R. Villar, R. Ortega-Hertogs, W. K. Park, and J. S. Moodera, J. Phys. D. 35, 1761 (2002).

[16] F. Guo, G. McKusky, and E. D. Dahlberg, Appl. Phys. Lett. 95, 062512 (2009).

[17] In this experiment, the time the magnetic field reaches the field of interest is defined as t=0.

[18] J. L. Snoek, Physica (Amsterdam) 5, 663 (1938). See Physics of Magnetism by S. Chikazumi and S. H. Charap, (Robert E. Krieger, Malabar, FL, 1964), chapter 15.

[19] In figure 2.5d Barkhausen jumps are observed. These jumps are generally observed in our junctions with the switching of the hard layer. Theses observed discrete jumps coexist with the logarithmic evolution of time.

[20] L. B. Steren, A. Barthélémy, J. L. Duvail, A. Fert, R. Morel, F. Petroff, P. Holody, R. Loloee, and P. A. Schroeder, Phys. Rev. B 51, 292 (1995)

[21] Z. Q. Lei, G. J. Li, William F. Egelhoff, Jr., P. T. Lai, and Philip W. T. Pong, IEEE Trans. Mag. 47, 602 (2011); W.F. Egelhoff Jr., P.W.T. Ponga, J. Ungurisb, R.D. McMichaelb, E.R. Nowakc, A.S. Edelsteind, J.E. Burnetted, G.A. Fischerd, Sensors and Actuators A 155 (2009) 217

Chapter 3:

Tunneling Conductance of Magnetic Tunnel Junctions

3.1 Introduction: the observations of conductance features

The magnetoresistance of magnetic tunnel junctions (MTJs), consisting of two ferromagnetic layers sandwiching a thin tunnel barrier, is governed by the relative orientation of the magnetizations of the ferromagnets. In general, tunnel junctions are ideal to study spin dependent transport and related tunneling physics. The famous Julliere's two-spin current model [1] captures the main features of the magnetoresistance effect in a simple fashion. Interface related effects, energy dependent densities of states (DOS) and more detailed electronic structures, however, have found to be necessary to completely describe spin dependent tunneling processes. The accounting for interfacial effects in MTJs has been shown repeatedly in various experiments [2, 3]. Additionally, LeClair *et al* [4] and Oepts *et al* [5] have observed a non-monotonic behavior in the bias dependent conductance of AlO_X based MTJs (see Fig. 3.1) which only appears for electrons tunneling in one

direction. LeClair *et al* concluded this was related to the electrode texturing and attributed this to band structure and density of states effects. The interfacial and band structure effects have been difficult to observe and resolve from each other without intentionally engineering the interface since transport measurements merely give a highly blended combination of the density of states of two spin channels, the band structure, barrier properties, interfacial bonding characteristics and other effects.

Despite these difficulties, we will show a fairly pronounced structure in the differential conductance at nonzero bias voltage which can be systematically controlled. While the feature is similar to that observed by LeClair, Oepts and colleagues, to our knowledge this is the first report showing this abnormal conductance feature can be controlled in a systematic way: the position and appearance of the conductance feature were tuned by the oxidization process. For a junction with a given barrier thickness, the voltage of the conductance feature decreases with increasing oxidization time. Investigation of the oxidization conditions at the interfaces on each side of the barrier was determined by X-ray photoelectron spectroscopy (XPS). Three types of materials for the electrodes had been explored. Furthermore junctions with different barrier thicknesses were studied and gave consistent results. In the end, we summarize all the results and discuss how this conductance feature is associated with the oxidization condition and possibly the band structure at one of the barrier interfaces.

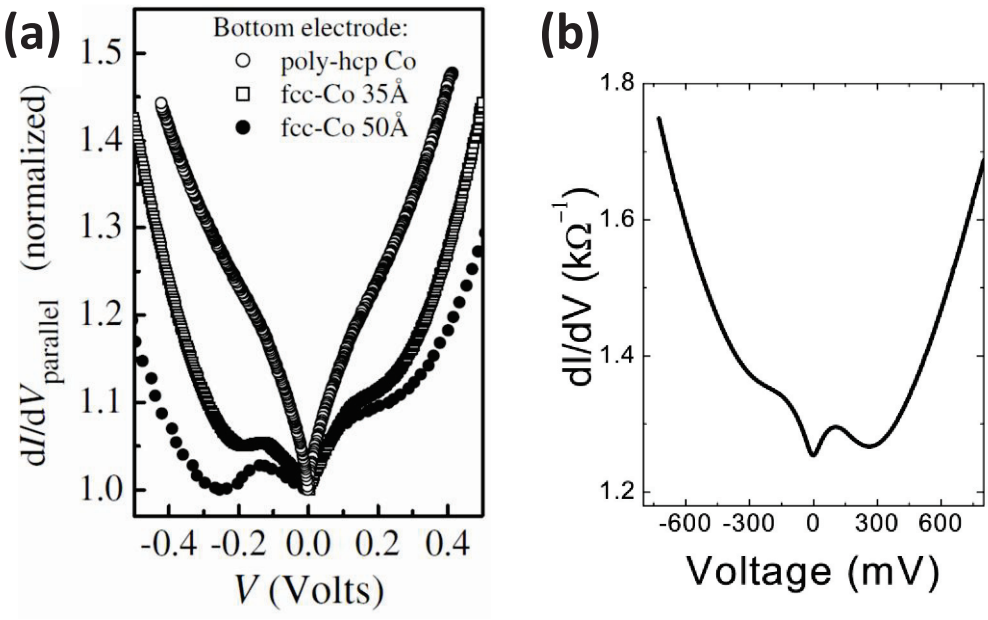

Figure 3.1

(a) Voltage dependent differential conductance data from P. LeClair et al PRL,*88*,107201 (2002). A similar conductance feature to that in our junctions (b) has been found for junctions with fcc-Co electrodes. All conductance curves above were measured in P-state. The conductance features in (a) and (b) occur in opposite voltages due to different sign definition: in both cases, the conductance feature is present when electrons tunnel from bottom to top electrodes.

3.2 Oxidization dependence of the conductance feature

The magnetic tunnel junctions for this conductance study were made in a DC magnetron sputtering chamber with a base pressure of about 4×10^{-8}Torr (as were those for the noise studies). Unless otherwise noted, the structure of the samples is Ta(20) /$Ni_{81}Fe_{19}$(4) /$Ir_{20}Mn_{80}$(8) /$Co_{90}Fe_{10}$(3) /Al(1.5) +oxidaztion/ $Co_{90}Fe_{10}$(1.5)/ $Ni_{81}Fe_{19}$(3) /Ta(10) where all the numbers represent the thickness of the layers in nm.

The formation of the alumina barrier was assisted by a plasma generated with an aluminum target in either in the sputtering chamber or a separate chamber without breaking the vacuum. A mixed gas of 5mTorr argon and 5mTorr oxygen were used during the oxidation process. The MTJs were post-deposition annealed at a temperature of 240°C for one hour. The junctions were patterned using photolithography and ion milling techniques; the junction dimension varied from $10\times10\mu m^2$ to $35\times35\mu m^2$. Four-point-contact transport measurements were taken with an Adler-Jackson bridge [6, 7].

First off, to study the oxidization process and its role in MTJs, a set of CoFe/AlOx/CoFe junctions were fabricated with various oxidation times: 40, 65, 80, 120, 180 seconds. Room temperature TMR (at zero bias) and resistance-area (RA) product for a series of junctions are plotted in Fig. 3.2. For these samples with an Al thickness of 1.5nm before oxidization, the TMR peaks around 120s indicating optimized oxidation. A shorter oxidization time may lead to incomplete oxidization of the aluminum at one interface corresponding to a lower TMR probably caused by the reduced spin polarization; however for a very long time the bottom CoFe electrode will be oxidized which will also reduce the TMR. In terms of the resistance, the RA product changes monotonically with oxidation time which indicates the effective barrier thickness increases with increasing oxidization time. Figure 3.2 provides a measure of the oxidization degree for a given oxidization setup and condition.

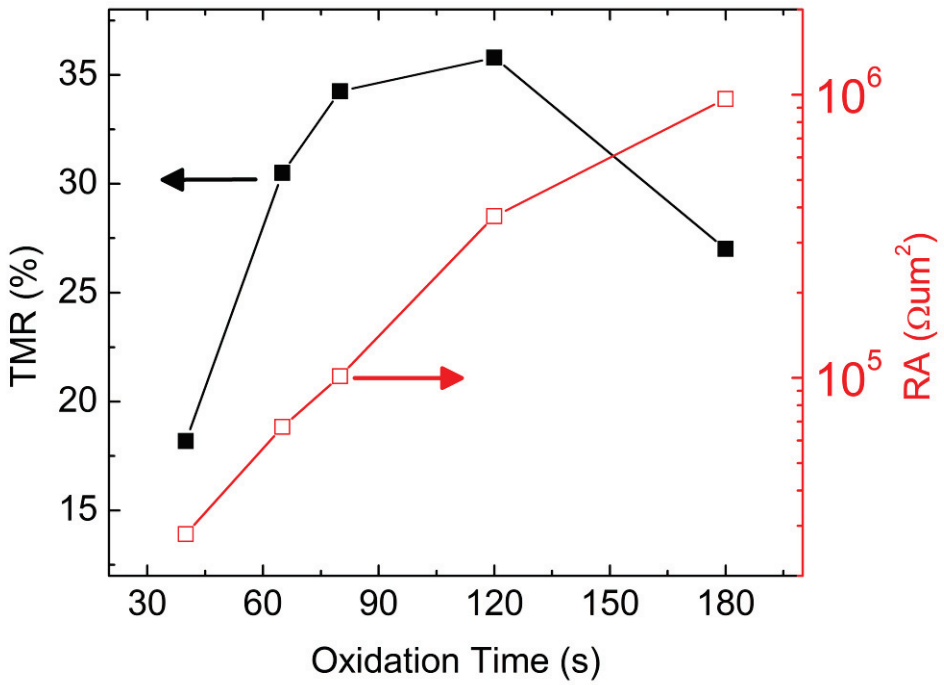

Figure 3.2

A series of CoFe/AlOx/CoFe junctions have been made with varies oxidation time. The graph above shows the room temperature TMR (solid black) and RA product (hollow red) as functions of oxidization time.

While measuring the voltage dependent differential conductance (dI/dV) for the same samples, a pronounced feature was observed for some of the junctions. Fig. 3.3 shows the conductance normalized to that at zero voltage, $^{dI/dV}/_{dI/dV|_{V=0}}$, measured at 77K. Positive bias corresponds to electrons tunneling from the bottom electrode to the top electrode. Except for the most oxidized junction (180s), the conductance curves are clearly asymmetric about zero bias voltage – a local maximum and a minimum were found when electrons tunnel from the bottom to the

top electrode. The correlation between the appearance of the conductance feature and current direction is a common feature in all reported AlO_X based tunnel junctions as I will discuss later. Furthermore, the position for this feature is also sensitive to the oxidization time. Shorter oxidization times display the feature at the higher bias voltages. This can be seen in Fig. 3.3 where the maxima of the conductance feature are shown.

One may also notice from Fig 3.3 that the general curvature is less for shorter oxidization time samples compared to longer oxidization time samples. This effect is attributed to the effective barrier thickness: shorter oxidization time yields a thinner barrier width and therefore the conductance will be less voltage dependent. In other words, the I-V curve will be more linear. The barrier profile dependence as well as its effect on the conductance feature will be discussed in more detail in section 3.7.

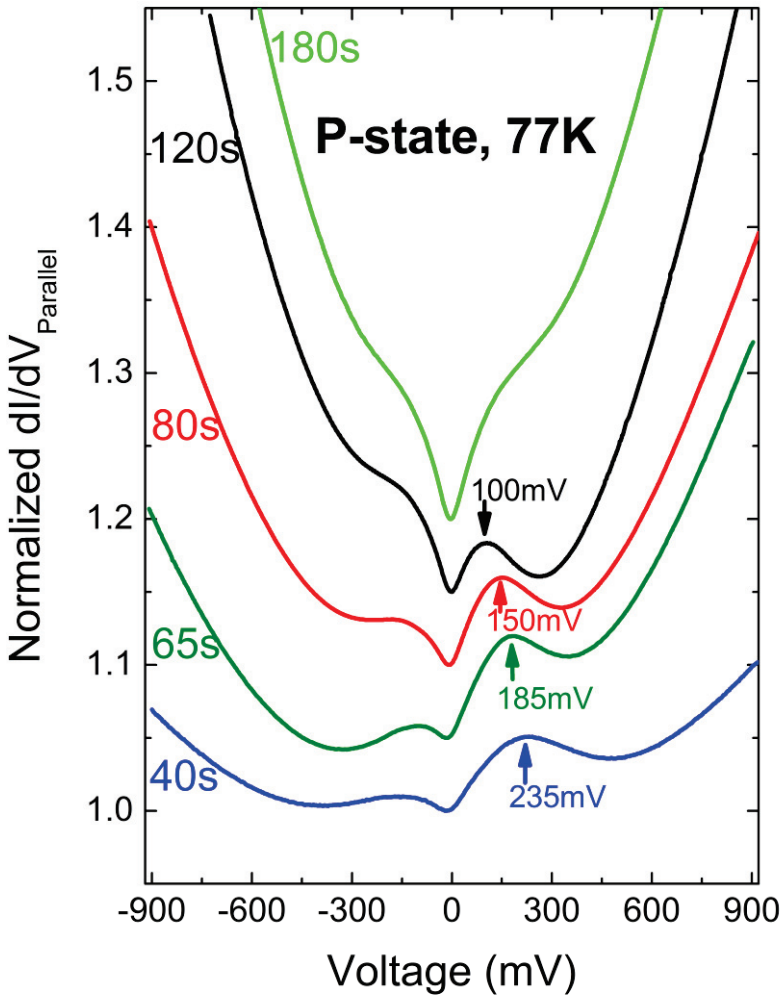

Figure 3.3

Bias dependent differential conductance (parallel state) for the junctions in Fig.3.2 with different oxidation times (labeled beside each curve) measured at 77K. The data are normalized by zero voltage conductance so that $dI/dV|_{V=0}=1$. A 0.5 vertical displacement is added between each curve for clarity. The voltages labeled for the 40, 65, 80 and 120s curves are the positions of the conductance maxima obtained by taking $d^2I/dV^2=0$.

3.3 X-ray photoelectron spectroscopy (XPS) – a surface probe

Since the presence of the conductance feature depends on the oxidization process as described in previous section, an X-ray photoelectron spectroscopy (XPS) experiment was done to investigate the chemical states at the barrier-electrode interfaces. Two series of samples were prepared separately for this study on the barrier interfaces.

The first group of samples used to study the barrier top interface had a structure of Ta(8) /AlOx(1.5nm Al) /CoFe(1.5) /Ta(0.5) and an oxidation time ranging from 0 to 180s using exactly the same oxidation procedure as the MTJs discussed above. As one can see in the XPS spectra (Fig. 3.4a), the metallic cobalt peak is always present as are the peaks associated with the Co-O bonding. Despite the various oxidization times, the CoFe layer on top of the AlO_X barrier was always partially oxidized, even for the shortest oxidization time of 30s. Because aluminum and oxygen forms stronger bonds than Co-O, one does not expect unoxidized metallic aluminum at the top interface. The iron signals are relatively week due to the low composition of Fe (10%) in CoFe alloy and buried in a large Auger background the signals become difficult to detect.

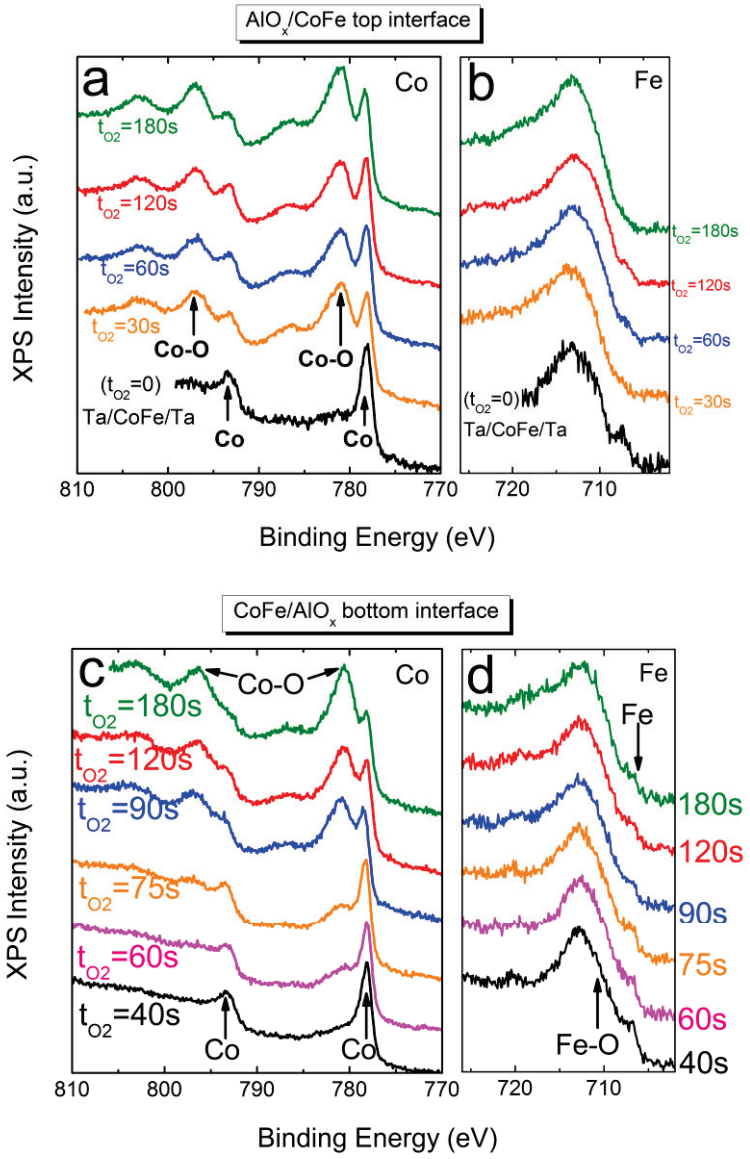

Figure 3.4

X-ray photoelectron spectroscopy data of Co and Fe signals. Samples shown in (a) and (b) with a structure of Ta(8nm) /AlOx(1.5nm Al) /CoFe(1.5nm) /Ta(0.5nm) were prepared to study oxidization conditions on top interface. The CoFe electrode is partially oxidized for all nonzero oxidization times. Samples in (c) and (d), Ta(8) /NiFe(4) /IrMn(8) /CoFe(3) /AlOx(1.5nm Al), were prepared to study the bottom interface; contrary to the top interface, the oxidization degree of CoFe metal changes gradually with increasing oxidization time.

A second group of samples, Ta(8) /NiFe(4) /IrMn(8) /CoFe(3) /AlOx(1.5nm Al), were fabricated to investigate the bottom interface. Unlike the top interface, the Co-O peak intensity changes gradually with oxidization time for the bottom interface. As can be seen in Fig. 3.4c, the Co spectrum of the 40s sample changes little from the metallic film with little trace of oxidization. The Co-O peak gradually increases with oxidization time and becomes strongest for 180s.

The results of chemical states at the two barrier-electrode interfaces are summarized in Fig. 3.5, where the relative Co-O signal intensity ($I_{Co\text{-}O}/I_{Co}$) is shown as a function of oxidization time. For the top interface, the electrode is always partially oxidized and the signal magnitude is independent of oxidization time. For the bottom interface, the electrode stays in metallic state for short oxidization times but is eventually oxidized at longer oxidization times.

Comparing the XPS experiment with previous conductance data, one can see that for long oxidization times, both the top and bottom interfaces of the barriers have formed bonds with the oxygen resulting in a symmetric chemical state on either side of the barrier. This situation is consistent with the symmetry observed in the conductance for long oxidation times, where no feature has been found. For samples with shorter oxidization times, the bottom interface has little to no oxide (metallic or under oxidized aluminum against the interface) while the top interface, independent of the oxidization time, is oxygen rich and contains Co that is partially oxidized. This gives rise to an asymmetry in the barrier interface and coincides with the asymmetry in transport measurements including the abnormal conductance feature. As suggested from the XPS results, the bottom CoFe-AlO_X interface appears to be responsible for the conductance feature. I will further discuss, later in the chapter, that this conclusion is consistent with several other independent experiments.

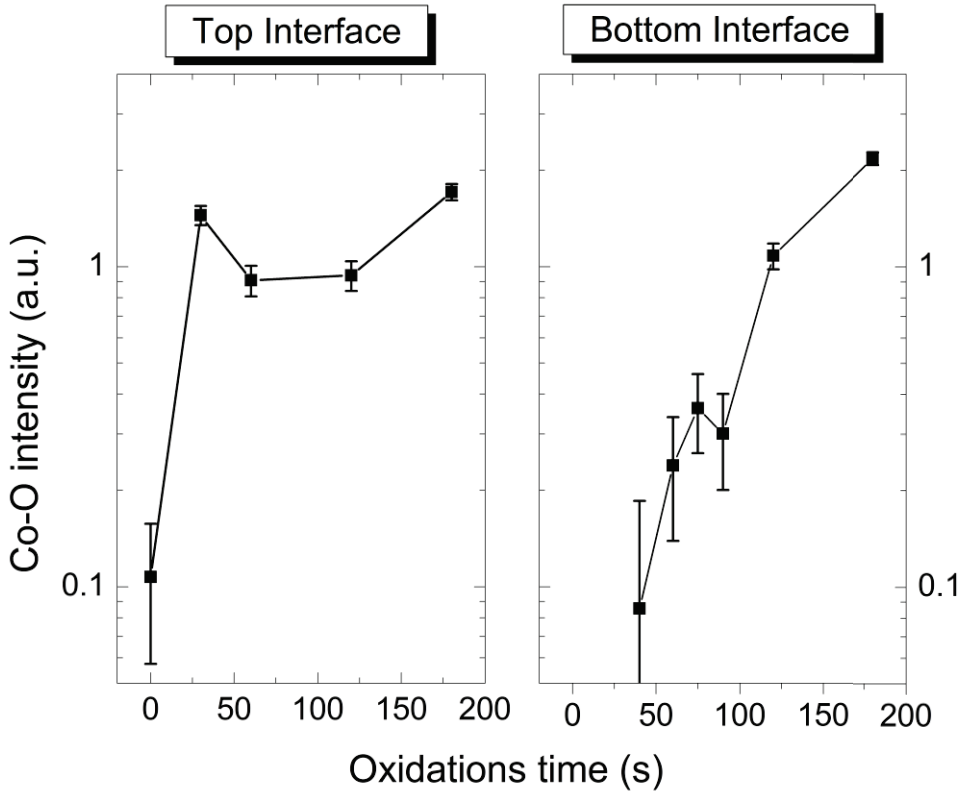

Figure 3.5

Intensity of cobalt-oxygen bonding, defined by the peak intensity ratio of Co-O to Co from Figs. 3.4a and 3.4c, as a function of oxidization time for both top and bottom interfaces.

3.4 Electrode material dependence

So far only CoFe/AlO_X/CoFe junctions have been discussed. One interesting aspect of the problem that has not been touched is the material dependence of the conductance feature. To study this effect, a set of samples with a combination of three different electrodes were fabricated. First, tunnel junctions consisting of NiFe/AlO_X(t_{O2}=90s)/CoFe (bottom/insulator/top) were made with the same layers above the barrier but a different bottom electrode. Although one expects to see the

conductance feature with an oxidization time of 90s for CoFe/AlO_X/CoFe junctions, the conductance data shown in Fig. 3.6 is fairly symmetric and featureless; however when the top electrode was replaced by either NiFe or Ni and the bottom structure remained the same, the conductance feature can be reproduced at positive bias voltage. Therefore, for all the materials investigated, only a CoFe bottom electrode can reproduce the conductance feature while the choice of the material for the top electrode does not play a direct role in the feature. Once again, this provides direct evidence that it is the bottom CoFe/AlO_X interface, rather than the top interface, that is responsible for the conductance feature.

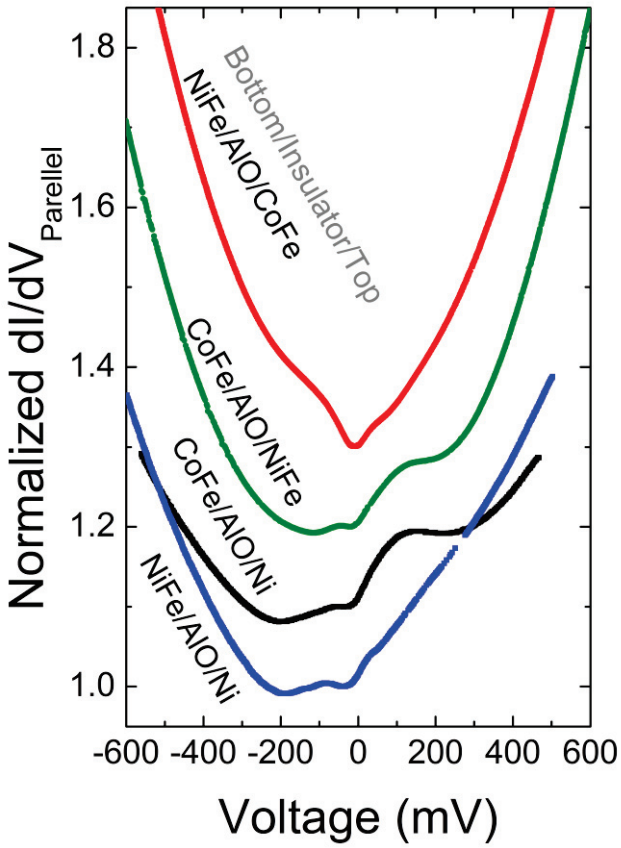

Figure 3.6

Normalized bias dependence of conductance for three witness samples with different electrodes measured at 77K: the red curve is NiFe/AlO_X(1.5nm Al with t_{O2}=90s)/CoFe; the green curve is CoFe/AlO_X (1.5nm Al with t_{O2}=90s)/NiFe; black is CoFe/AlO_X(1.5nm Al with t_{O2}=100s)/Ni; and the blue curve is from a sample with a structure of NiFe/AlO_X(1.5nm Al with t_{O2}=100s)/Ni. A vertical spacing of 0.1 between each curve is applied for clarity.

3.5 Barrier thickness dependence

The junctions in section 3.1 all had the same aluminum thickness prior to oxidization. For those samples, by changing the oxidization time, the state of the CoFe/AlO_X bottom interface was varied and the conductance feature was shown to disappear at high levels of oxidization. In this section, I will discuss a very similar idea yet a different approach of tuning the bottom interface and therefore the conductance feature. Instead of using the same aluminum thickness, a wedge of Al was deposited before the oxidization. This was done by moving the substrate relative to the aluminum target during deposition, as depicted in Fig. 3.7. The same oxidization condition was applied across the entire substrate and it was then patterned resulting in samples with various barrier thicknesses having the same oxidization time.

Fig. 3.8 shows how tunneling magnetoresistance (TMR) ratio and resistance area (RA) product vary with the aluminum thickness. Similar to the fixed barrier width sample set in Fig. 3.2, there is s maximal TMR for an optimal thickness of around 1.5nm. Samples thinner or thicker than this thickness suffer from over- and under-oxidization respectively. The RA product increases with the aluminum thickness as one would expect. It is worth noting that the bare aluminum thickness before oxidization may not be proportional to the effective barrier thickness when oxidized. With the same oxidization time applied, the resulting oxidization degree/condition is not expected to be the same for MTJs with different aluminum thicknesses, which is why as the aluminum layer thickness changes from 1.4 to 2.0nm but the junction resistance increases only by about one order of magnitude.

In order to study the conductance data and find a correlation between the barrier thickness and the conductance feature, the normalized bias dependent conductance

data is plotted in Fig. 3.9. The feature shows a strong barrier thickness dependence, even though the bottom electrodes for all junctions should share the same crystallinity, texture, as well as other qualities. For a given oxidization time, the junctions with a thin barrier experience complete or over-oxidization: the bottom CoFe/AlO_X interface is likely to have oxide and there metallic aluminum is not expected. No conductance feature or asymmetry in conductance curve has been found in these thin junctions. This is similar to the fixed aluminum thickness samples with long oxidization times (Figs. 3.2 and 3.3), where no feature was seen in the conductance data either.

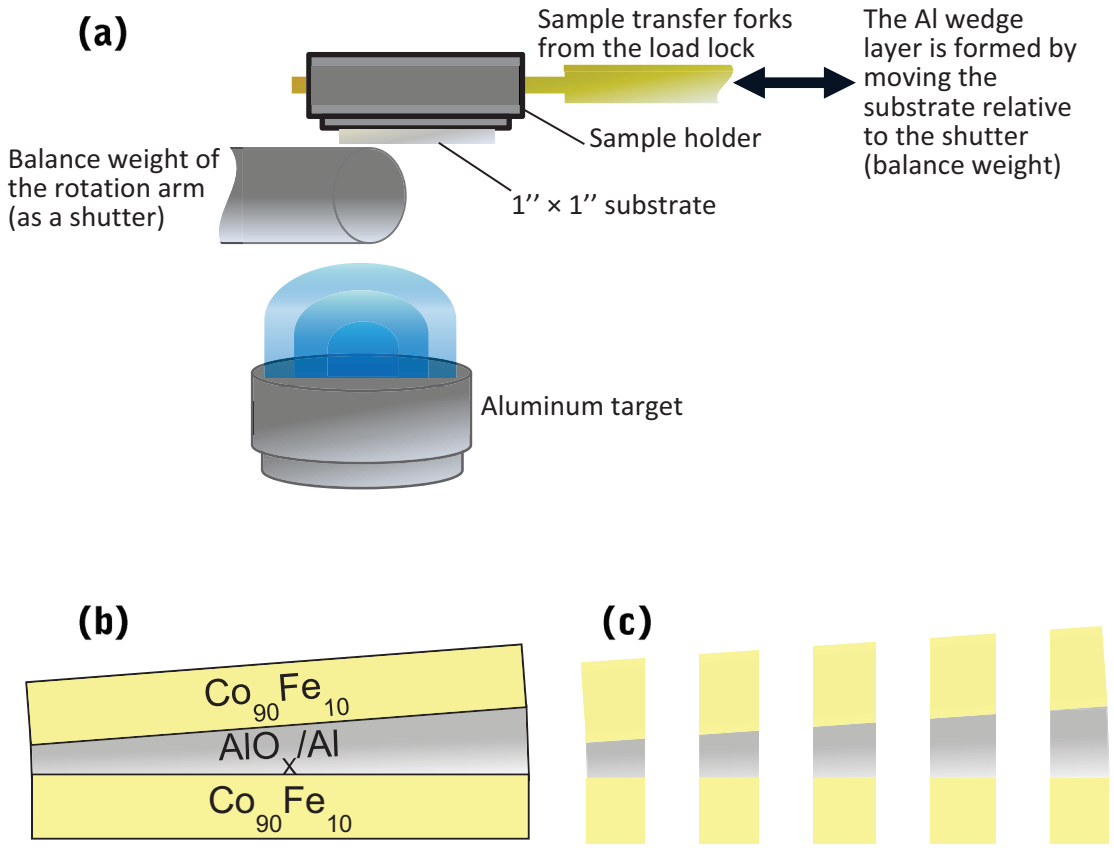

Figure 3.7

(a) An illustration showing the method to form the aluminum wedge layer; (b) a cartoon of a MTJ structure with a wedged barrier; after the thin film was patterned a series of tunnel junctions with various barrier thickness were formed as shown schematically in (c).

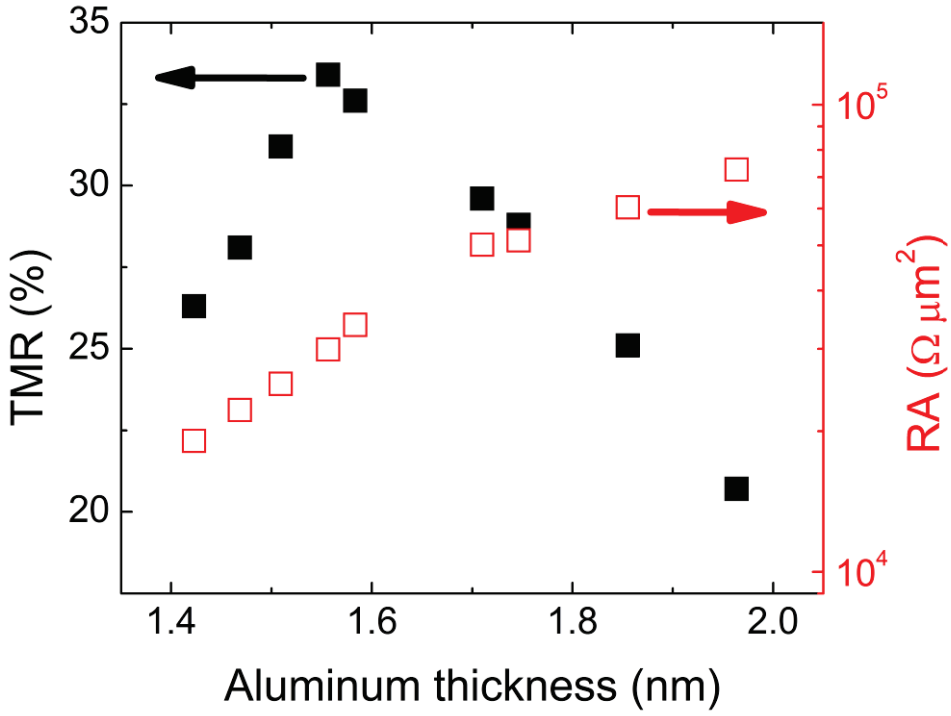

Figure 3.8

Tunneling magnetoresistance (TMR) ratio and resistance area (RA) product as functions of barrier thickness (aluminum thickness before oxidization) for the wedged samples. Same oxidization condition was applied to all the samples.

As the barrier thickness starts to increase, the bottom interface becomes more likely to be metallic for a given oxidization time. The conductance feature develops around 300mV (see the 1.47nm sample in Fig. 3.9), and it becomes fairly pronounced as the barrier thickness continues to increase (1.56nm sample and beyond). For these samples, the barrier carries an asymmetry at least in terms of the chemical state: the top interface is partially oxidized while the bottom interface is in a more metallic state. This interfacial asymmetry results in the conductance feature and gives rise to the asymmetry in transport measurements. This situation is similar to oxidizing a

fixed aluminum thickness samples for a short or moderate time (Figs. 3.2 and 3.3), where the barrier is also asymmetric and the conductance feature was observed, despite the different barrier thickness. In summary, two methods have been used to vary the state of the bottom interface, fixing the aluminum thickness and varying the oxidization time or fixing the oxidization time and varying the barrier thickness. Both approaches were consistent in showing a barrier symmetry dependent conductance feature.

One more aspect displayed in Fig. 3.9 is that for some of the thickest barriers (especially 1.86nm, 1.96nm samples) the conductance feature, though still present, is less pronounced. This may sound contradictory since we have learned that the more metallic the bottom interface is the more obvious the conductance feature should look. Though correct by itself, this statement overlooks the fact that the effective barrier thickness changes along with the interface condition. As the barrier becomes wider, the normalized conductance increases faster with the bias voltage, which results in a sharper curvature. This effect due to the barrier profile essentially changes the visual effect of the conductance feature. Even for the same density of state in the electrode and same interfaces' conditions, a wider barrier weakens the conductance feature (at least visually). More details of the barrier profile dependent conductance feature will be discussed later in this chapter.

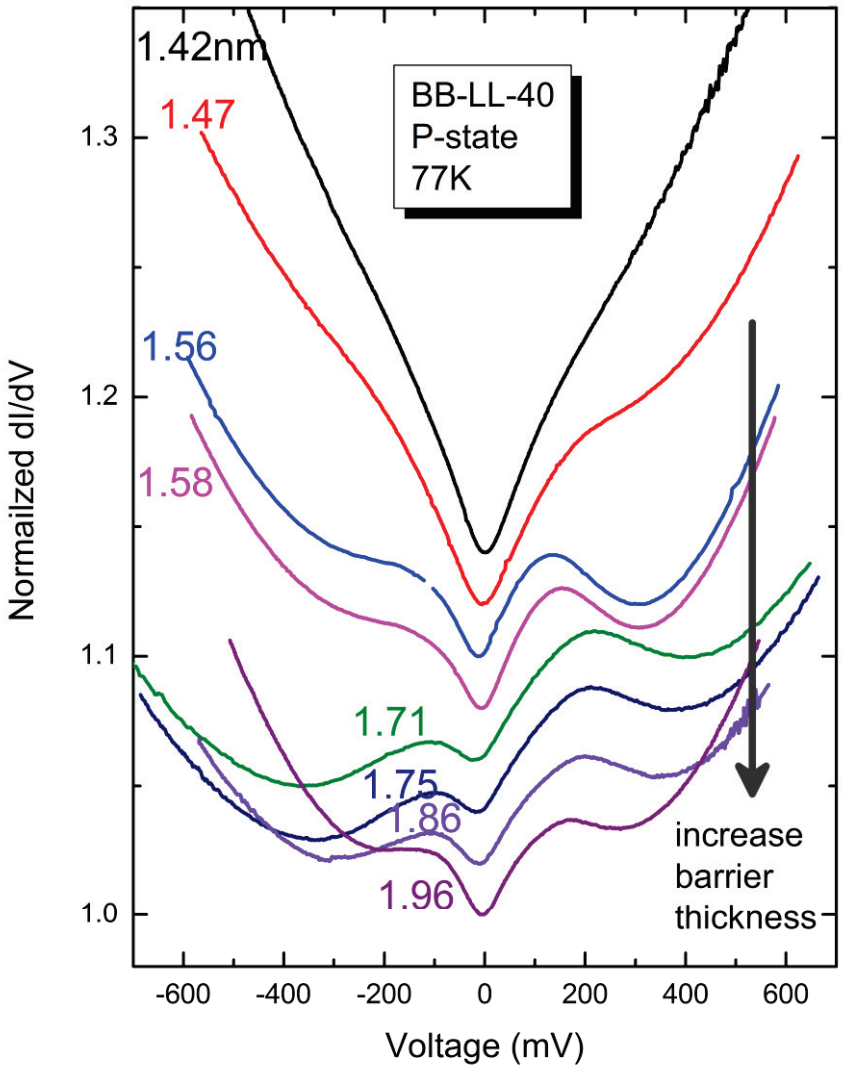

Figure 3.9

A series of normalized bias dependent conductance curves for the wedged samples in the parallel state. Vertical displacement is applied for clarity. The numbers indicate the aluminum layer thickness (before oxidization) for each curve.

3.6 Explorations on the origins of the conductance feature

In this section, I will discuss the possible explanations for the conductance feature by summarizing the experimental results and by comparing similar features from other works. This is followed by a discussion of the influence of band structure/density of states on the voltage dependent conductance. At the end of the section, a calculation of the conductance is introduced to explore the effects from both the density of states and the barrier profile.

Independently from the XPS data and from the electrode varying experiment, it is clear that the bottom CoFe/AlO_X interface is responsible for the conductance feature that we observed. The metallic state of the bottom interface appears to correlate with the presence of the conductance feature. Furthermore, the conductance feature only occurs when electrons tunnel from the bottom to the top electrode but not the other direction. This is consistent with all other reported conductance features in AlO_X based tunnel junctions [3, 4, 5, 8] (though the voltage signs and the current directions were defined differently by different groups). In one of these works, LeClair and coworkers [3] dusted copper at either the top or the bottom barrier interfaces of Co/AlO_X/Co tunnel junctions. When no copper was present, the control sample showed a conductance feature similar to that observed in our junctions when the electrons tunnel from the bottom to the top electrode. As the copper was dusted at the top interface, the TMR dropped by 80% as the dusting layer increasing from 0 to about 1nm caused by the spin scattering from copper, but the conductance feature remained unchanged. However, for the bottom dusted samples Co/Cu/AlO_X/Co, the conductance feature weakened with increasing Cu layer thickness and the feature vanished when the Cu layer was about 4Å thick. The fact that dusting copper only at the bottom interface, not at the top, affects conductance

feature is completely in agreement with our conclusion that the bottom interface is responsible for the feature.

Similar features in the conductance have also been observed in MgO based MTJs [9, 10]. In these works, a more detailed discussion focused on how the band structure influences voltage dependent conductance. To illustrate the argument in a simple fashion, a cartoon of the band structure for a specific electrode is shown Fig. 3.10. One spin band, marked black, has its band edge near the Fermi level. The distance between the band edge and the Fermi level is defined as V_{dip}. As the bias voltage increases from zero and the electrons start to flow from this electrode to the other side of the barrier, electrons in the black spin band in Fig. 3.10 contribute to the total conductance along with the electrons in other bands crossing the Fermi level. When the bias continues to increase and the Fermi level of the other electrode passes this band edge, or equivalently when $V_{bias} \geq V_{dip}$, this band will stop contributing to the total differential conductance. Consequently a dip in conductance will be present. In other words, V_{dip} reflects itself in the transport properties indicating the position of the conductance feature as labeled in Fig. 3.10. In this sense, the conductance measurement provides a way to determine the information about the band structure.

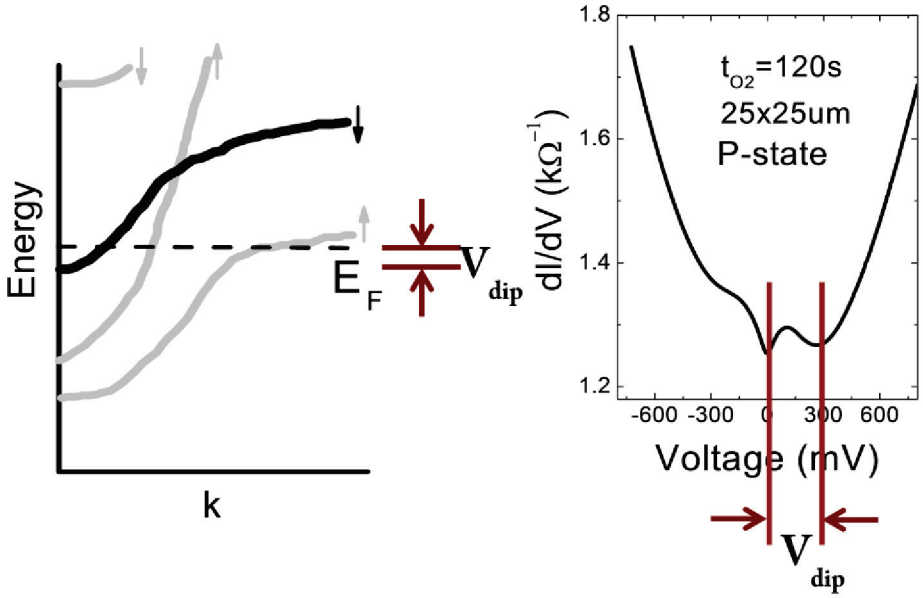

Figure 3.10

The left panel shows a schematic of the band structure of a given electrode with band edges closed to the Fermi level; the distance between the band edge below the Fermi level and the Fermi level, V_{dip}, also reflects in the location of the conductance feature, as shown in the right panel.

Based on the above argument, a band structure with at least one band edge located within the proximity of the Fermi level will lead to the conductance feature. This statement is supported by a few experiments [4, 11] in which the electrode texture/crystallinity (via a buffer layer or annealing) and therefore the band structure were varied. However, besides the band structure (or density of states) there is another requisite condition for the conductance feature: the chemical state of the bottom interface that can be controlled via oxidization. For example, in the wedged sample set in Figs. 3.8 and 3.9, all the junctions were made on the same substrate and thus one would expect that the crystallinity of the bottom electrodes for each

junction are very similar, if not identical. Nevertheless, due to different oxidization degrees of the bottom interface the presence of the conductance feature could be tuned.

So far for all AlO_X based junctions reported, there is an interesting common aspect: the conductance feature is pronounced only in one current direction, i.e. when the electrons tunnel from the bottom to the top electrode. The possible reasons for no feature associated with electrons flowing in the other direction are twofold. First, the electrode at the top interface is always found to be partially oxidized from XPS experiments (this is true at least for the metal film deposition and post oxidization method), and we have learned that the conductance feature is not present with a partially oxidized interface. Second, as a general rule of thin film growth, the crystal structure and texture are extremely seed layer dependent. Growing a thin film on top of an amorphous AlO_X layer should lead to an amorphous structure, if not polycrystalline [4], at least for the first a few atomic layers. Losing the regular crystalline structure will significantly alter the band structure and density of states [12], and therefore diminishes the corresponding features in transport measurements. (Note for epitaxial MgO junctions the conductance feature can be seen for both current directions [10, 11], indicating the top and bottom interfaces of MgO junctions are more symmetric than those of AlO_X junctions).

A test experiment has been done to further explore the latter reason (crystallinity/texturing). A layer of aluminum metal was dusted in between the top interface, giving a junction structure of CoFe/AlO_X/dusting Al/CoFe. The purpose of this dusting Al layer was to absorb the excessive oxygen so that the CoFe electrode could be isolated from these oxygen particles and remain metallic. With the new aluminum layer, the junction resistance increased due to a barrier thickness increase

and the TMR dropped due to the reduced spin polarization as one would expect. However, despite of the dusting Al layer (up to 5Å) protecting the top CoFe from becoming oxidized, there was no conductance feature in the current direction when the electrons tunnel to the bottom electrode. This is possibly because the top CoFe remained in the amorphous form [4], though maybe metallic, and thus would still not give rise to the conductance feature.

In summary, there are at least two requisite conditions needed to observe the conductance feature. Not only a particular band structure of the electrode is required, but also the electrode-barrier interface needs to stay mostly metallic in order to preserve the conductance feature.

3.7 Density of states and conductance calculations

Bias dependent tunneling conductance is a powerful tool to study the electronic structure and has played an important role in many fields in physics, including understanding and probing the density of states of superconductors. In the case of magnetic tunnel junctions, some sharp density of state peaks are located near Fermi level for some magnetic materials (i.e. Nickel) and the conductance measurement becomes a great tool to study the electronic structure [7].

The fundamental physics of the tunneling conductance, the calculation method and how the conductance reflects the density of states information are introduced in appendix A4. Here we take the calculated density of states data from B. Jones's group [13] and discuss how the density of states effect reveals itself in the tunneling

conductance and how it evolves with barrier shape. Figs.3.11b and 3.11c show the calculated I-V and conductance curves respectively for both P- and AP-states. Positive voltage is defined for electrons tunneling from the density of states in Fig.3.11a into a flat but polarized (polarization of 40%) density of states. Therefore by artificially making the density of states of one electrode flat, it becomes more straightforward to study how the density of states features in one electrode translates into the tunneling conductance.

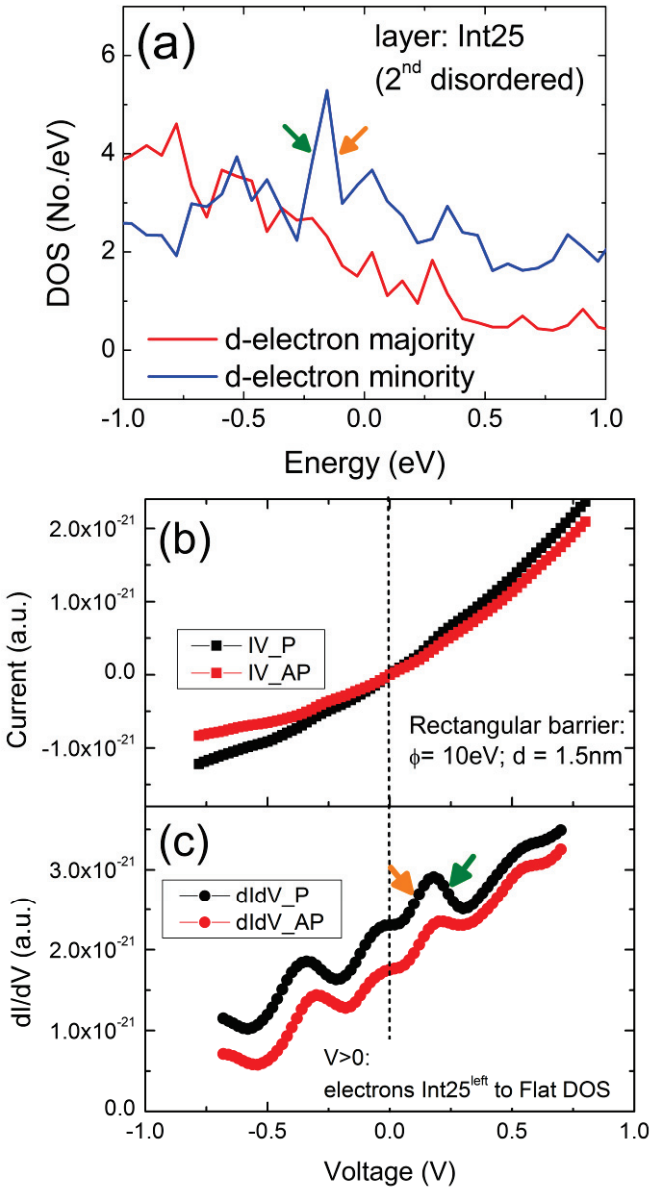

Figure 3.11

(a) Calculated density of states for two spin bands near the interface where there are mixture of aluminum (25%) and cobalt (75%). Data adopted from B.Jones *et al*'s calculation [13]. (b) Calculated current-voltage curves for P- and AP-states using the density of states in (a). (c) Calculated conductance data obtained from the 1st derivative of I-V data from (b).

There are two major features from the calculated conductance curves. First, the features in the density of states, i.e. peaks and valleys, do reproduce themselves in the differential conductance at some level. For example, in the region marked by the orange arrow (Fig.3.11c) a local increase in the conductance is located at around 0.2V. This was given rise from an increase in the density of states as the voltage swept to around 0.2V below the Fermi level, labeled by an orange arrow in Fig.3.11a. The same correlation is found between a drop in conductance and a decrease in the density of states as label by the green arrows in Figs. 3.11a and 3.11c. Hence, a feature in the density of states will tend to reproduce itself in the differential conductance. In this case (one electrode having a flat DOS), when the density of states effect dominates the measured conductance, the conductance curve becomes nearly a mirror image of the density of states about zero bias.

The second feature of the conductance curves is the tilted background (besides the parabolic shape from the barrier); the background is higher for positive voltages and lower for negative voltages. This shouldn't be a surprise considering the background in the density of states: as shown in Fig.3.11a, within the voltage range of interest (from -1 to 1 V) there are more states at lower energies and as the energy increases there are relatively fewer numbers of states available. This slow change in the density of states exactly translates to the conductance background.

Since experimentally one cannot separate the two spin channels and can only measure the total conductance, a feature (i.e. a peak or dip or sudden change in DOS) in either spin DOS can alter the conductance. However, it is possible to distinguish the contributions from the two spin bands by looking at the voltage dependent TMR, as plotted in Fig.3.12. A bump in TMR is seen at the positive voltage where the conductance feature occurs. This increased TMR suggests it is more likely

to have a peak in the majority spin (majority/minority spins are defined at Fermi level: $n_{majority}(E_F)>n_{minority}(E_F)$) density of states because a peak in minority spin density of states suppresses the TMR ratio. This also qualitatively agrees with the fact that the feature is more pronounced in the P-state rather than AP-state (see Appendix 4 for a more extensive discussion). Furthermore, this is consistent with calculated cobalt density of states at the interface (note the density of states are significantly different between interface and bulk) where the peak only appears in the majority spin (blue curve in 3.11a).

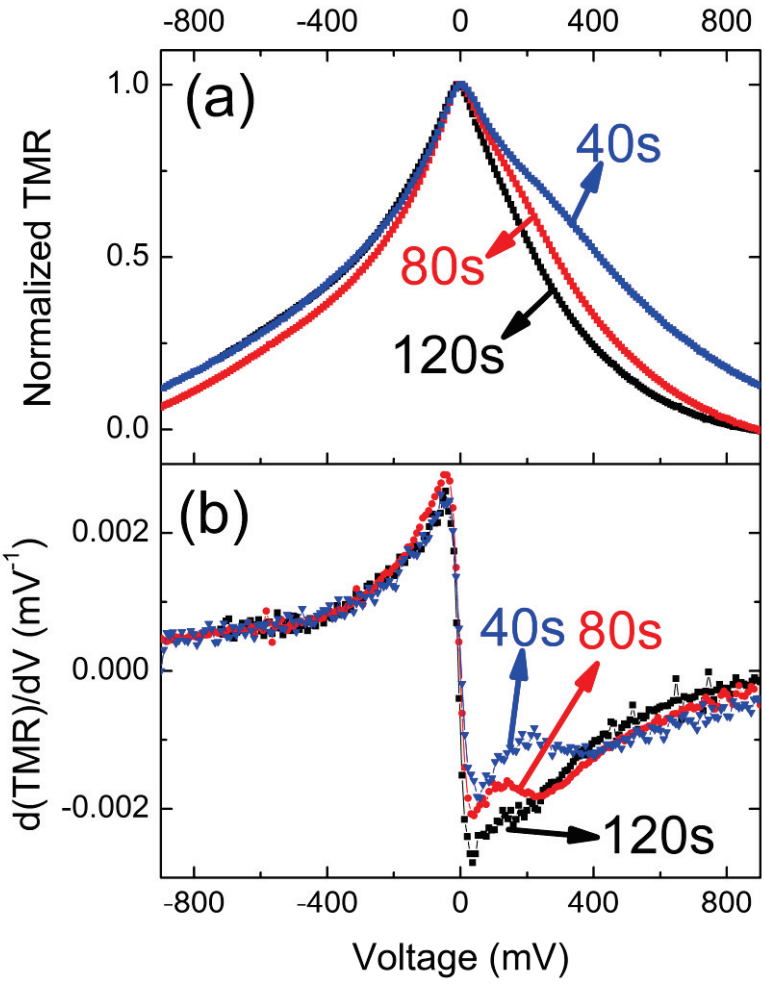

Figure 3.12

(a) Measured TMR vs. voltage for three samples with 40s, 80s, and 120s of oxidization times; (b) first derivative of TMR with respect to voltage to amplify the bump in TMR at positive bias where the conductance feature occurs.

Now let us take the barrier profile into consideration and see its effect on the conductance feature. A rectangular shape is assumed for the barrier, with an energy height ***ø*** and width ***d***. Using the density of states data from Fig.3.11a for one

electrode and flat density of states for the other, one can calculate the normalized conductance as plotted in Fig.3.13. Different combinations of ***ø*** and ***d*** were used. Panel (a) shows the barrier width dependence of the conductance and in panel (b) the barrier height was varied. The strength of the conductance feature gets visually weaker when either ***d*** increases or ***ø*** decreases. This is because there are two parts simultaneously contributing to the conductance, electronic structure (density of states) and the barrier shape. When the barrier profile effect becomes strong, the overall background of the conductance is strongly dependent on the voltage (I-V curve very non-ohmic or large curvature in dI/dV(V)), thus weakening the influence from the density of states. This can be achieved by either increasing ***d*** or decreasing ***ø***. Furthermore, even for a given barrier shape and a given density of states, the position of the conductance feature will cause a difference in the magnitude of the features in the conductance. For the DOS peaks having higher energies, their corresponding tunneling probabilities are higher than those DOS peaks having lower energies. A higher tunneling probability means a greater conductance, and therefore a DOS feature having higher energy will yield a stronger conductance feature than one located at the a lower energy (see the example in Appendix 4).

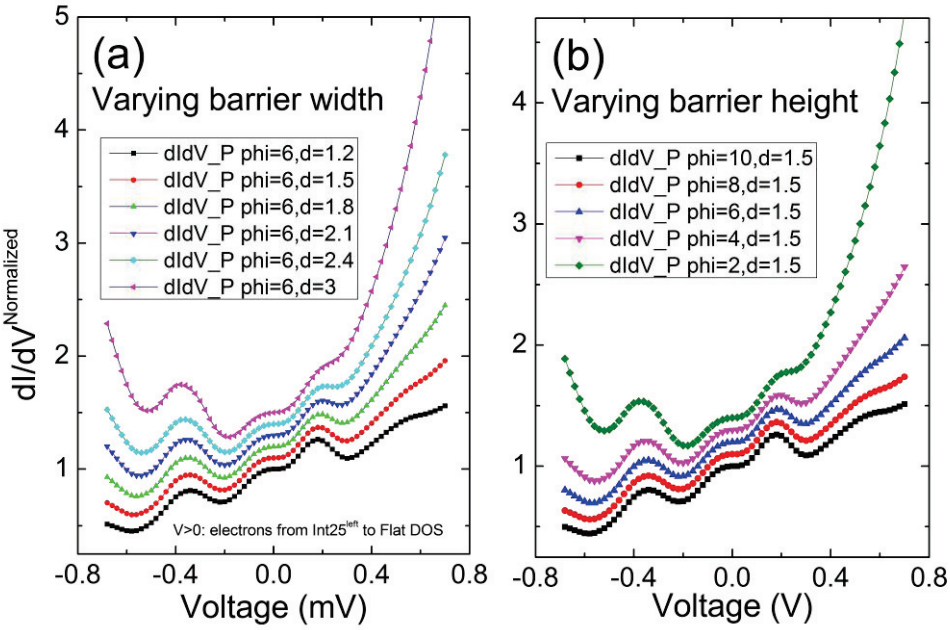

Figure 3.13

Normalized conductance as a function voltage for barriers with various widths (a) and various heights (b); the same density of states were used for all the conductance curves.

As mentioned in the introductory part of the chapter, the conductance is a measure of a variety of different effects all tangled together in a complicated way. However we have shown that it is possible to see the conductance evolving mostly due to one of the effects, such as the barrier shape or the density of states, by simply changing the oxidization time or barrier thickness. Increasing the oxidization time, for example, not only will partially oxidize the bottom interface therefore suppressing the conductance feature but also will increase the effective barrier thickness thus making the junctions less ohmic and weakening the conductance feature. It can be seen in Fig.3.3, where the samples with short and moderate oxidization times have flatter conductance curves and especially for the least oxidized junction, the conductance shows a tilted background at small voltages due to the decreasing density of states above the Fermi level. Consistent results are also observed for the wedged junctions

in Fig.3.9. As the barrier width increases for a given oxidization time, the bottom interface becomes more metallic. This is accompanied by the appearance of the conductance feature. As the barrier width continues to increase, however, the barrier effect starts to play an important role, causing stronger voltage dependence of the conductance and thus weakening the conductance feature. In conclusion, mixed effects from both the density of states and the barrier profile are not only seen in the calculations but also showed up in our measurements.

To continue exploring the interface and the density of states effects in the MTJs, some possible experiments are proposed as discussed in the following. Due to a sharp DOS peak near E_F in nickel, the differential conductance curves of Ni-based MTJs have been observed previously by our lab to have a pronounced feature [7]. Based on those observations, one can further study the transition from CoFe-based to Ni-based MTJs by inserting a thin layer of Ni at the interfaces of CoFe/AlO_X/CoFe junctions. Therefore by varying the Ni thickness (t_{Ni}) in the junctions, CoFe/AlO_X/dusting Ni (t_{Ni})/CoFe, it is possible to observe the DOS effect evolving from the CoFe to Ni, since the DOS of the two are expected to be quite different. Furthermore, this also allows us to study the relevant length scale over which the transition occurs. Similarly, the conductance measurements can also be done by dusting CoFe at the interface of Ni junctions (CoFe/AlO_X/dusting CoFe (t_{CoFe})/Ni). To take one further step, inserting Ni at the interfaces of a CoFe/AlO_X/ dusting Ni (t_{Ni})/Normal metal is also a possible approach to understand the interface effect. The advantage of this experiment is that by varying t_{Ni} both regular junction-MTJ transition (by measuring the TMR ratio) and the DOS transition (by measuring the dI/dV) can be observed. The correlation of the two transitions may provide useful information of the tunneling process.

References

[1] M. Julliere, Phys. Lett. 54A, 225 (1975)

[2] E. Y. Tsymbal, O. N. Mryasov, and P. R. LeChair, J. Phys: Condens. Matter 15 (2003) R109-R142 (section 3.6)

[3] P. LeClair, H. J. M. Swagten, J. T. Kohlhepp, and W. J. M. de Jonge, Appl. Phys. Lett. 76, 3783 (2000)

[4] P. LeClair, J. T. Kohlhepp, C. H. van de Vin, H. Wieldraaijer, H. J. M. Swagten, W. J. M. de Jonge, A. H. Davis, J. M. MacLaren, J. S. Moodera, and R. Jansen, Phys. Rev. Lett. 88, 107201 (2002)

[5] W. Oepts, M. F. Gillies, R. Coehoom, R. J. M. van de Veerdonk and W. J. M. de Jonge, J. Appl. Phys. 89, 8038 (2001)

[6] J. G. Adler and J. E. Jackson, Rev. Sci. Instrum. 37, 1049 (1966)

[7] G. McKusky, *Density of states effects in nickel based magnetic tunnel junctions.* Ph.D. Diss. University of Minnesota, 2009. Dissertations & Theses @ CIC Institutions, ProQuest. Web. 4 Aug. 2011 (Publication Number: AAT 3387288)

[8] M. Jourdan, A. Conca, C. Herbort, M. Kallmayer, H. J. Elmers, and H. Adrian, J. Appl. Phys. 102, 093710 (2007)

[9] Wenhong Wang, Enke Liu, Masaya Kodzuka, Hiroaki Sukegawa, Marec Wojcik, Eva Jedryka, G. H. Wu, Koichiro Inomata, Seiji Mitani and Kazuhiro Hono, Phys. Rev. B, 81, 140402(R) (2010)

[10] F. Greullet, C. Tiusan, F. Montaigne, M. Hehn, D. Halley, O. Bengone, M. Bowen, and W. Weber, Phys. Rev. Lett., 99, 187202 (2007)

[11] "The effect of annealing on the spin-transfer torques of MgO MTJ nanopillars", Yun Li, Hsin-wei Tseng, Pinshane Huang, John Read, Dan Ralph and Robert Buhrman, APS march meeting 2011

[12] Li Gao, Xin Jiang, D. M. C. Nicholson, Teya Topuria, and Stuart S. P. Parkin, Appl. Phys. Lett., 95, 012508 (2009).

[13] T. Tzen Ong, A. M. Black-Schaffer, W. Shen, and B. A. Jones, Phys. Rev. B, 82, 054429 (2010)

Bibliography

Z. Q. Lei, G. J. Li, William F. Egelhoff, Jr., P. T. Lai, and Philip W. T. Pong, IEEE Trans. Magn. ***47***, 602 (2011)

G. McKusky, *Density of states effects in nickel based magnetic tunnel junctions.* Ph.D. Diss. University of Minnesota, 2009. Dissertations & Theses @ CIC Institutions, ProQuest. Web. 4 Aug. 2011 (Publication Number: AAT 3387288)

M. N. Baibich, J. M. Broto, A. Fert, F. Nguyen Van Dau, F. Petroff, P. Etienne, G. Creuzet, A. Friederich, and J. Chazelas, Phys. Rev. Lett. ***61***, 2472 (1988)

G. Binasch, P. Grunberg, F. Saurenbach, and W. Zinn, Phys. Rev. B ***39***, 4828 (1989)

M. Julliere, Phys. Lett. ***54*** (1975) 225

J. S. Moodera, L. R. Kinder, T. M. Wong, and R. Meservey, Phys. Rev. Lett. ***74***, 3273, (1995).

E. Y. Tsymbal, O. N. Mryasov, and P. R. LeChair, J. Phys: Condens. Matter 15 (2003) R109-R142

J. S. Moodera and G. Mathon, J. Magn. Magn. Mater. ***200*** (1999) 248

J. S. Moodera, J. Nassar and G. Mathon, Annu. Rev. Mater. Sci. 1999. ***29***: 381-432

S. S. P. Parkin, Annu. Rev. Mater. Sci. 1995, ***25***: 357

E.Y.Tsymbal and D.G.Pettifor, Solid State Physics, ***56***, 113 (2001)

M.B. Weissman, Review of Modern Physics, ***60*** (1988) 537

C. Dekker, A.J. Scholten, F. Liefrink, R. Eppenga, H. van Houten, and C.T. Foxon, Phys. Rev. Lett. ***66***, 2148 (1991)

A.H. Steinbach, J.M. Martinis, and M.H. Devoret, Phys. Rev. Lett. ***76***, 3806 (1996)

L. Jiang, E. R. Nowak, P. E. Scott, J. Johnson, J. M. Slaughter, J. J. Sun, and R. W. Dave, Phys. Rev. B. ***69***, 054407 (2004).

C. Ren, X. Liu, B. D. Schrag, and G. Xiao, Phys. Rev. B. ***69***, 104405 (2004).

S. Ingvarsson, G. Xiao, S. S. P. Parkin, W. J. Gallagher, G. Grinstein, and R. H. Koch, Phys. Rev. Lett. ***85***, 3289 (2000).

D. Mazumdar, X. Liu, B. D. Schrag, M. Carter, W. Shen, and G. Xiao, Appl. Phys. Lett. ***91***, 033507 (2007).

D. Mazumdar, X. Liu, B. D. Schrag, W. Shen, M. Carter and G. Xiao, J. Appl. Phys. ***101***, 09B502 (2007).

D. Mazumdar, W. Shen, X. Liu, B. D. Schrag, M. Carter and G. Xiao, J. Appl. Phys. ***103***, 113911 (2008).

A. F. Md Nor, T. Kato, S. J. Ahn, T. Daibou, K. Ono, M. Oogane, Y. Ando, and T. Miyazaki, J. Appl. Phys. ***99***, 08T306 (2006).

R. Guerrero, F. G. Aliev, R. Villar, R. Ortega-Hertogs, W. K. Park, and J. S. Moodera, J. Phys. D. ***35***, 1761 (2002).

F. Guo, G. McKusky, and E. D. Dahlberg, Appl. Phys. Lett. ***95***, 062512 (2009).

J. L. Snoek, Physica (Amsterdam) 5, 663 (1938).

S. Chikazumi and S. H. Charap, (Robert E. Krieger, Malabar, FL, 1964), chapter 15.

L. B. Steren, A. Barthélémy, J. L. Duvail, A. Fert, R. Morel, F. Petroff, P. Holody, R. Loloee, and P. A. Schroeder, Phys. Rev. B ***51***, 292 (1995)

Z. Q. Lei, G. J. Li, William F. Egelhoff, Jr., P. T. Lai, and Philip W. T. Pong, IEEE Trans. Mag. ***47***, 602 (2011)

W.F. Egelhoff Jr., P.W.T. Ponga, J. Ungurisb, R.D. McMichaelb, E.R. Nowakc, A.S. Edelsteind, J.E. Burnetted, G.A. Fischerd, Sensors and Actuators A ***155*** (2009) 217

M. Julliere, Phys. Lett. ***54A***, 225 (1975)

P. LeClair, H. J. M. Swagten, J. T. Kohlhepp, and W. J. M. de Jonge, Appl. Phys. Lett. ***76***, 3783 (2000)

P. LeClair, J. T. Kohlhepp, C. H. van de Vin, H. Wieldraaijer, H. J. M. Swagten, W. J. M. de Jonge, A. H. Davis, J. M. MacLaren, J. S. Moodera, and R. Jansen, Phys. Rev. Lett. ***88***, 107201 (2002)

W. Oepts, M. F. Gillies, R. Coehoom, R. J. M. van de Veerdonk and W. J. M. de Jonge, J. Appl. Phys. ***89***, 8038 (2001)

J. G. Adler and J. E. Jackson, Rev. Sci. Instrum. ***37***, 1049 (1966)

M. Jourdan, A. Conca, C. Herbort, M. Kallmayer, H. J. Elmers, and H. Adrian, J. Appl. Phys. ***102***, 093710 (2007)

Wenhong Wang, Enke Liu, Masaya Kodzuka, Hiroaki Sukegawa, Marec Wojcik, Eva Jedryka, G. H. Wu, Koichiro Inomata, Seiji Mitani and Kazuhiro Hono, Phys. Rev. B, ***81***, 140402(R) (2010)

F. Greullet, C. Tiusan, F. Montaigne, M. Hehn, D. Halley, O. Bengone, M. Bowen, and W. Weber, Phys. Rev. Lett., ***99***, 187202 (2007)

Yun Li, Hsin-wei Tseng, Pinshane Huang, John Read, Dan Ralph and Robert Buhrman *"The effect of annealing on the spin-transfer torques of MgO MTJ nanopillars"*, APS march meeting 2011

Li Gao, Xin Jiang, D. M. C. Nicholson, Teya Topuria, and Stuart S. P. Parkin, Appl. Phys. Lett., ***95***, 012508 (2009).

T. Tzen Ong, A. M. Black-Schaffer, W. Shen, and B. A. Jones, Phys. Rev. B, ***82***, 054429 (2010)

Ya.M. Blanter and M. BuK ttiker, Physics Reports ***336*** (2000) 1-166

G. Lecoy and L. Gouskov, Phys. Status Solidi ***30***, 9 (1968)

R. Guerrero, F. G. Aliev, Y. Tserkovnyak, T. S. Santos, and J. S. Moodera, Phys. Rev. Lett. ***97***, 266602 (2006)

S. Zhang, P. M. Levy, A. C. Marley and S. S. P. Parkin, Phys. Rev. Lett., ***79***, 3744 (1997)

Appendix 1:

Magnetic Tunnel Junction Photo Patterning Procedures

1. Depositing tunnel junctions on a substrate for subtractive processing at the NFC:

- Use Si substrates coated with 200nm SiN_4 and clean them by sonicating in acetone and (soapy) DI water and repeat 3 times. The acetone removes the protective layer of photoresist applied prior to cutting the wafer on the wafer saw as well as other organic dirt. Go to NFC to spin on headway spinner and spray acetone and then IPA on the substrate to remove any other particulates. Prebake the substrate for ~1min at 105C. Check under the microscope (dark field mode) to ensure the surface of the substrate is free of impurities or dust.
- The sample is sputtered in a growth field (~2kOe) produced by two permanent magnets on the sides of the sample holder. This field sets the exchange coupling between the anti-ferromagnet and ferromagnet.
- The junction structure is shown as follows: Ta 20nm/ NiFe 4.5nm/ IrMn 8nm/ CoFe 3nm/ Al (t)/ CoFe 1.5nm/ NiFe 3nm/ Ta 10nm. All the ion milling times listed in this

standard operating procedure refer to this structure. This has been shown to give a ~600Oe exchange bias field as deposited.

- The oxidation of the alumina tunnel barrier is done in the load lock as follows:

  - Put the sample into the load lock after depositing the aluminum and close the gate valve to the main chamber.
  - The Pirani and Penning gauges MUST be turned off using the on/off switch on the back of the control box. NEVER operate a hot filament vacuum guage or pump with a vacuum pump that uses a hydrocarbon based oil when pure oxygen is involved, it could be catastrophic.
  - Partially close the manually operated gate value between the load lock and the turbo pump.
  - Set the partial pressure for Ar and O_2 gases with the leak valves (typically 5mTorr Ar and 5mTorr O_2). There are two capacitance manometers on the load lock which have operating ranges of 10^{-4} to 1 Torr and 1 to 1000 Torr. Make sure the argon gas goes to the load lock.
  - Upon the pressure is stabilized, light the plasma using the target gun in the load lock.
  - Once oxidation is complete switch off the power supply to remove the plasma, and close all the leak valves.
  - Open the gate value and switch the rough and turbo pump back on as if pumping down from atmosphere as described in the big chamber SOP. After the load lock pressure is < 2E-6Torr, send sample back into the main chamber and deposit the top metallic layers. Switch the needle valves beneath the main chamber to make sure the argon supply goes to the main chamber.

- When annealing the sample, make sure the annealing field has the same direction as the growth field: i.e. the + and – signs on the sample holder and oven are consistent. An anneal of 265C for 1-2 hours is typical. An easy way to check the effect of the

anneal on the exchange bias is to make a GMR device with the same exchange bias structure and check the GMR curve before and after a anneal.

2. Photo pattern to define the bottom electrodes

- Clean the chip: spin on headway spinner and spray acetone and then IPA on the substrate to remove any particulates. Then prebake the substrate for ~1min at 105C. (always do this step before applying photoresist to remove water from the surface)
- Apply photo resist S1805 and spin for 30 seconds at 3krpm, then bake for ~1min at 105C.
- Using the Maba6 in soft contact mode with an exposure time of 2.5secs and a 40um gap expose mask I. Ensure the alignment marks look good before etching
- Ion mill ~18mins to make sure it etches all the way through the metal layers to the substrate. Ion mill 3 minutes and turn off the power supply for a ~1.5 minute cool time. This cooling step prevents the photoresist from baking on, and allows the photoresist to be easily removed with acetone. Repeat until 18 minutes (may vary) is reached. Look at the sample through the view port at the end of every three-minute mill to see the color of the substrate. It should start to look purple at ~14 minutes, and be totally purple by 18 minutes with the MTJ stack listed in the beginning of this SOP. Be especially careful to watch the argon pressure when ion milling; keep it within 8.8 –9 E-5 Torr. You will find that the mill rate is very sensitive to small changes in the operating pressure.
- Remove photoresist by soaking in acetone for at least five to ten minutes and then sonicating for 5 minutes.
- Look at the features under a microscope to check the cleanliness and sharpness of the features.

3. Photo pattern to form top electrode.

- Pattern the junction area (brown) with photoresist (mask#2) and ion mill for ~11mins (may vary) so that it etches down to the bottom layer, i.e. the Ta layer. It is very important to get the alignment correct for this step. Do this mill like the first in steps of 3 minutes on and 1.5 minutes off.
- Clean off the photoresist using the same procedure as listed in step 2.
- Junction area should be visible under a microscope. Do not be surprised if the bottom electrode looks purple or not quite metallic. There is most likely still metal to contact to and it is an optical effect in that extremely thin metallic layers are somewhat transparent and you are seeing the purple silicon nitride beneath the metal.
- This step relies heavily on the thick (20nm) tantalum seed layer to give a wide margin for error when doing the 2nd ion mill. The idea is to mill through the tunnel barrier, but to still have the bottom electrode there to connect to the contact pads later.

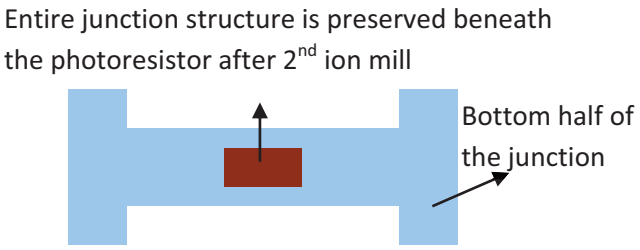

Figure A1.1: Schematic after second ion mill

4. Cover the entire chip with SiN_4. The features will be clearly visible even with 100nm of SiN4 covering them.

- PECVD: make sure it is ready for nitride and temperature is within 10C of 100C; use program sin100
- If the interior of the PECVD is full of junk, i.e. particulate matter it may be necessary to O2 clean the chamber prior to use.

- Deposition time: 8 mins at ~ 12.5nm / minute gives ~100nm.

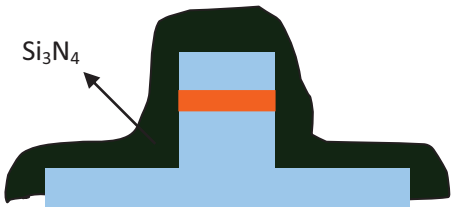

Figure A1.2: Entire substrate is cover with a layer of insulator

5. Cover the brown area with photoresist (alignment is crucial for this step so that the bottom and top electrodes are only electrically connected through the tunnel junction)

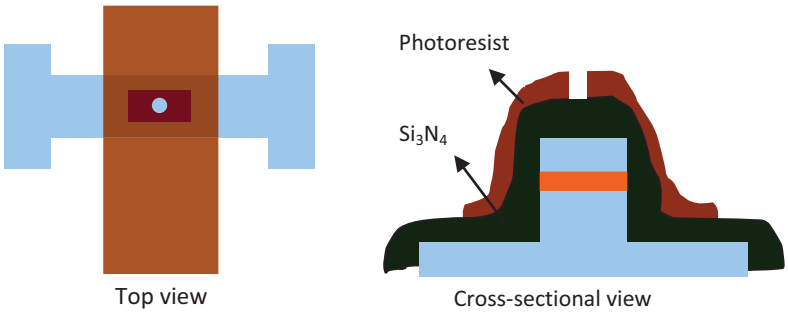

Figure A1.3: Patterned photoresist ready for reactive ion etch

6. Etch away the SiN4 that is not covered by the resist

- STS etcher: use recipe TYB-TEST, 5mins. The reactive ion etch (RIE) rate is highly sensitive to the sample being etched. Cited rates can be off by as much as an order of magnitude.
- Clean off the photoresist
- Ion mill for 1min to clean the surface prior to sputtering the electrical contacts.

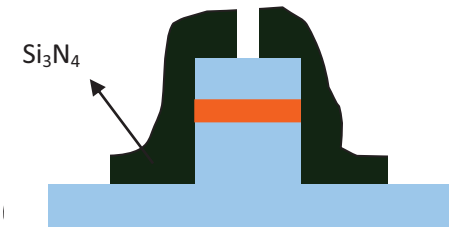

Figure A1.4: Schematic after RIE

7. Immediately put the samples into the load lock then transfer them to the main chamber and sputter with Aluminum after 1 minute ion mill.

- Set dc power supply to 80 watts
- Sputter for 10mins at lowest height of 82mm.

8. Apply photoresist to pattern the top and bottom electrodes (brown areas.) The features will still be clearly visible through the aluminum.

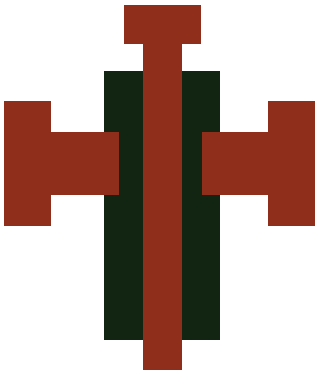

Figure A1.5: Photoresist is patterned to moved unwanted aluminum

9. Use Trion II to etch away uncovered Al

- Load sample into Trion first.
- Load file: Al
- Wait until the patterned Al becomes well-defined 4-5 minutes. Sample is visible through port on top of Trion II.
- Clean off the resist

*An alternative way for step 9 is to use wet etch:

- Spin coat with 1813 at 3~4krpm for 30sec, then expose with soft contact mode and 40um gap for 5~6 sec
- Develop with 351/H_2O for 25 sec (note the 351 developer also etches Al so it is not suitable for very thin Al; use MicroDev:H_2O=1:1 (available in Crowell's group) for thin Al film)
- Soak in CD26 for 2-3min and check under a microscope to be sure the Al features are sharp and top/bottom electrode are completely separated (be aware CD26 will slowly eat photoresist especially for long etch time)
- The wet etch is more convenient but has about 2um edge effect (undercut)

Appendix 2:

Shot Noise in Magnetic Tunnel Junctions

1. Background

Shot noise is the electric current fluctuation in a dc current due to both the quantization of charge carriers and the random (uncorrelated) arrival times of the carriers. Though insignificant in many cases due to the extremely small charge of the electron, it is detectable. On the contrary, measurements of shot noise have been found to be a powerful and unique tool. This is particularly true for a great deal of mesoscopic systems in condensed matter physics, since shot noise provides useful information ranging from carrier charge to electron-electron interactions and from carrier transmission to electron coherence properties [1].

Shot noise which is independent of frequency depends only on the charge and dc current level and can be described by the following equations:

for current fluctuations: $S_I = 2eI$ (units: I^2/Hz);

for voltage fluctuations: $S_V = 2eVR$ (units: V^2/Hz).

It is most convenient for us to measure the voltage power spectral density (PSD), S_V; therefore the second equation is more relevant. In some cases, the measured shot noise may deviate away from the value expressed by the above equations for reasons such as the correlation between the electrons. In order to account for the deviation, a quantity referred to as the Fano factor, ***F***, is introduced and it is defined as $F = S_V^{measured}/2eVR$; when F=1, the shot noise is fully Poissonian; and when F<1 or F>1 (very rare), the shot noise is sub- or super-Poissonian [1].

For normal metal-insulator-normal metal tunnel junctions, the transmission of which is well at zero limit due to the tiny tunneling coefficient, shot noise is almost always the value predicted by the above equations [1] (F=1), and therefore measuring the shot noise of the tunnel junctions has become a common method of noise calibration especially at low temperatures. However, shot noise in magnetic tunnel junctions (MTJs) has received less attention. In this Appendix, I will compare the shot noise in MTJs to that in non-magnetic tunnel junctions, and determine whether the magnetic configuration could affect the measured shot noise, and most importantly consider how we can understand shot noise in MTJs.

2. Measurement of shot noise in magnetic tunnel junctions

In order to measure shot noise, the bias voltage was varied. Since Johnson (thermal) noise only depends on the junction resistance and the temperature and is

independent of the voltage or the current, the change in frequency independent noise due to the increasing voltage can only be caused by shot noise. Fig.A2.1 shows a typical response of the noise spectrum to the voltage. 1/f noise appears at the lowest frequencies (below 10^4Hz), the magnitude of which scales with V^2; at higher frequencies, where the spectra are flat, the noise level increases with voltage due to shot noise.

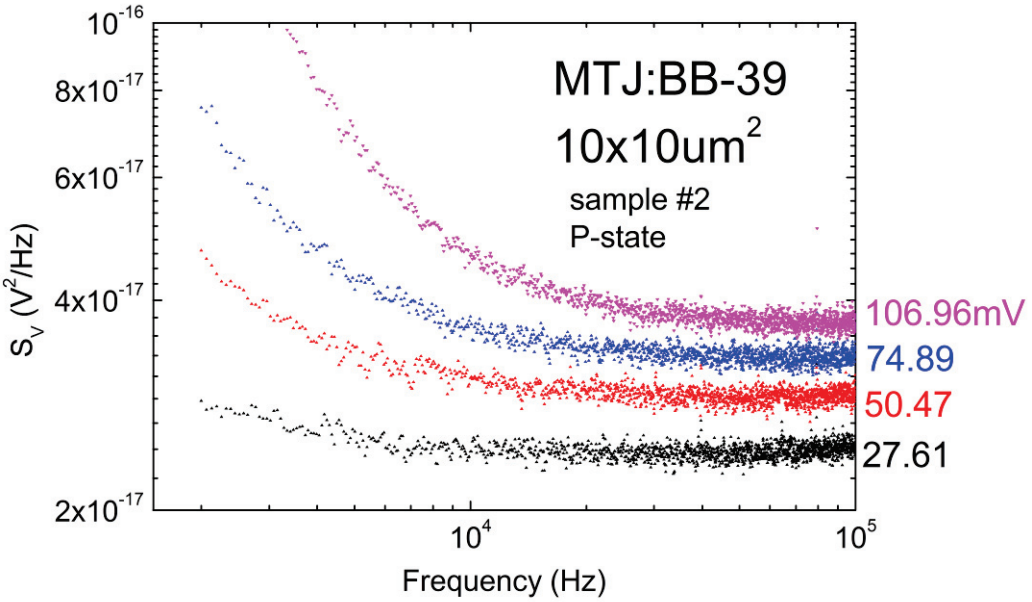

Figure A2.1

Example of the noise spectra with various bias voltages for a MTJ set in P-sate

A plot of high frequency noise level (white noise) vs. voltage, such as the one shown in Fig.A2.2, allows one to study the shot noise. The background noise (i.e. from the preamplier) remains constant with increasing voltage, and the shot noise changes linearly with the voltage as expected. Finding the slope of S_V(V) and using the equation $S_V = F \cdot 2eVR$, the Fano factor ***F*** can be obtained. The example in Fig.A2.2

gives Fano factors of the MTJ in the P-state at both positive and negative voltages, and in either case the measured Fano factor is approximately one.

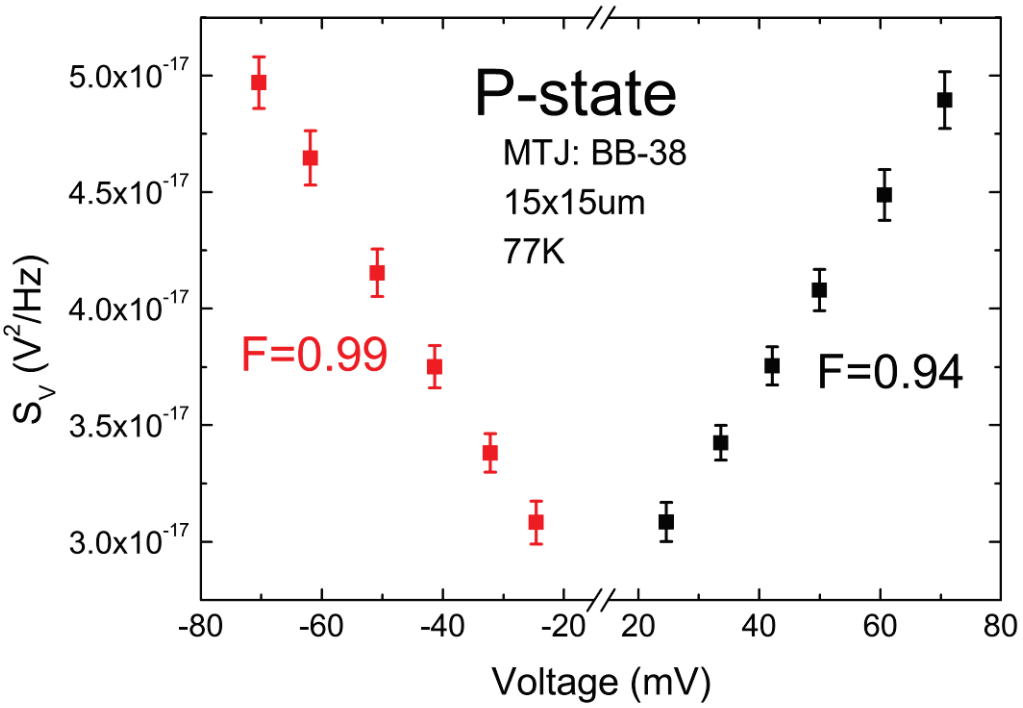

Figure A2.2

Voltage dependent high frequency (white) noise levels; the Fano factors labeled are given by the linear fit.

Several precautions need to be taken for shot noise measurements. First, for our setup the bias voltage is increased by decreasing the variable resistor (see Fig.2.1). At high bias, the condition $R_{variable} >> R_{sample}$ maybe not be valid anymore. The measured noise $S_V^{measured}$ will not be equal to the noise from the sample S_V^{sample} and the equation for the junction noise needs to be modified:

$$S_V^{sample} = S_V^{measured} \left(\frac{R_{variable}}{R_{variable}+R_{sample}}\right)^2.$$

Second, for some samples the change in junction resistance with voltage is not negligible, so it cannot be treated as constant for computing the Fano factor. Finally, the linear relation between the white noise level and the voltage does not hold at small voltages, where the total white noise results from a combination of Johnson and shot noise. The complete equation for white noise (Johnson and shot noise) in tunnel junctions is [2]: $S_V = 2eRVcoth(\frac{eV}{2k_BT})$. For $V>V_c=4k_BT/e$ ($V_c\approx26$mV at 77K in the measurements) the PSD equation can be reduced to $S_V = 2eRV$ which is exactly the equation for shot noise. When $V<V_c$, the noise level becomes voltage independent and is dominated only by Johnson noise which is $S_V = 4k_BTR$.

To investigate the magnetic state dependent shot noise, the angle, θ, between the two electrode magnetizations were varied and the Fano factor measurement as in Fig.A2.2 was repeated for the each angle (positive bias, defined for the electrons tunneling from the bottom to top electrode, was applied for this experiment). The junction resistance as a function of the angle was also measured simultaneously, as an indicator of the magnetic state. For these experiments 8 MTJs were measured and all showed similar behavior, shown in Fig.A2.3. For zero angle the MTJ is in the P-state indicated by the low resistance, and the value of the Fano factor is in the vicinity of unity. As the angle increases, the junction undergoes a transition from the P- to AP-state with increasing resistance. The Fano factor, however, decreases with increasing angle, and reaches a minimum value of about 0.7 in the AP-state for the sample in Fig.A2.3. Though all junctions measured do not have exactly the same Fano factor vs. angle curve, the general results that $F_P \geq F_{AP}$ and that the Fano factor never exceeds one (in the suppressed shot noise region) are repeatable.

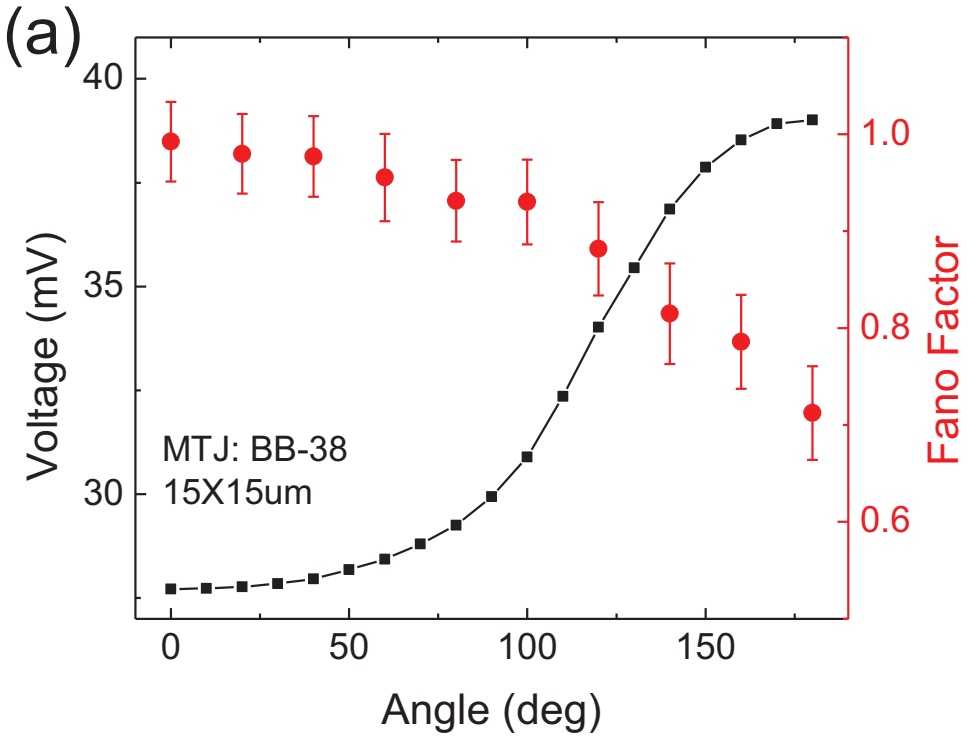
(a)
Voltage (mV)
Fano Factor
Angle (deg)
MTJ: BB-38
15X15um
40
35
30
1.0
0.8
0.6
0
50
100
150

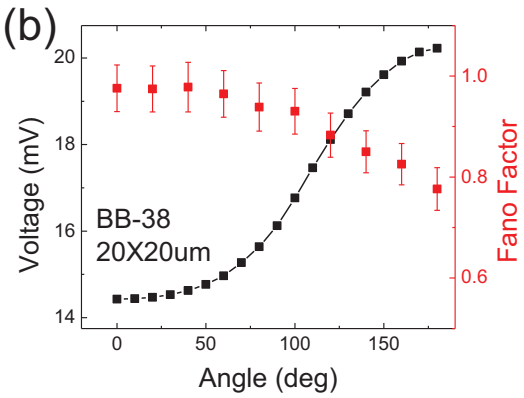
(b)
Voltage (mV)
Fano Factor
Angle (deg)
BB-38
20X20um
20
18
16
14
1.0
0.8
0.6
0
50
100
150

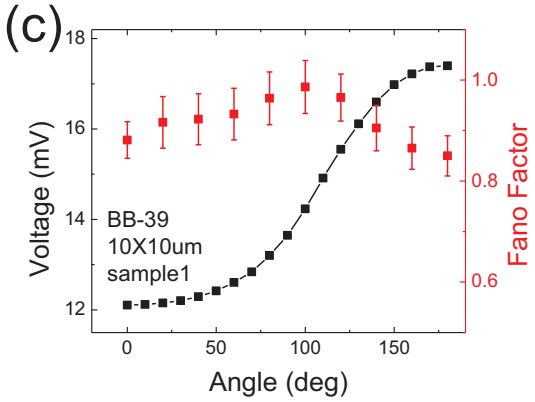
(c)
Voltage (mV)
Fano Factor
Angle (deg)
BB-39
10X10um
sample1
18
16
14
12
1.0
0.8
0.6
0
50
100
150

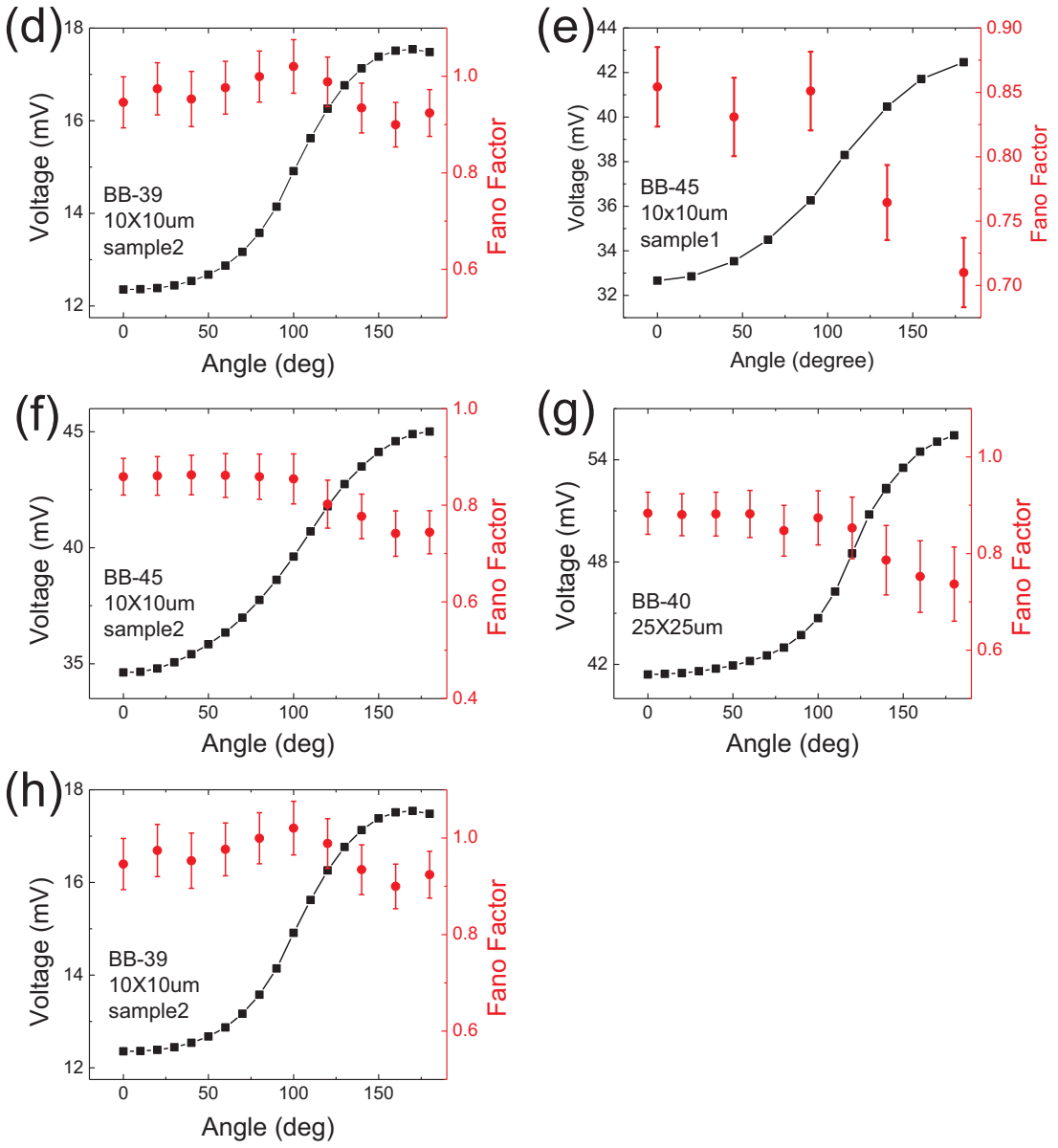

Figure A2.3

Voltage (black) and Fano factor (red) as functions of the angle between the magnetizations. (a) shows the sample as in Fig. A2.2 and the results of all other samples are displayed in (b)-(h).

3. Modeling the shot noise

To understand the variation of shot noise (Fano factor) with regards to the magnetic state, one model was proposed as a possible candidate to explain the noise behavior in MTJs [1, 3]. An impurity or an island is assumed to exist inside the tunnel barrier so that the electrons can tunnel from one electrode to this impurity site and continue to tunnel across the entire barrier to the other electrode, as shown in Fig.A2.4. For simplicity, two identical electrodes are assumed and thus they have the same spin polarization. In the parallel orientation, the resistances are $R_{\uparrow}^{left}=R_0$, $R_{\uparrow}^{right}=\beta R_0$, $R_{\downarrow}^{left}=\alpha\gamma R_0$, and $R_{\downarrow}^{right}=\alpha\gamma\beta R_0$. Several constants are introduced here: β accounts for the asymmetry of the barrier, or equivalently the position of the impurity site. For example, when β=1 the impurity is located at the center of the barrier and if β is greater (or less) than 1 the impurity sits on the left (or right) side of the barrier. α accounts for the resistance difference between spin up and spin down electrons. γ gives the population ratio of the spin up to spin down electrons. For arbitrary angle θ, $R_{\uparrow}^{left}$ and $R_{\downarrow}^{left}$ remain the same as those in the P-state, while $R_{\uparrow}^{right} = {2\alpha\beta R_0}/{\alpha+1+(\alpha-1)cos\theta}$ and $R_{\downarrow}^{right} = {2\alpha\beta\gamma R_0}/{\alpha+1-(\alpha-1)cos\theta}$.

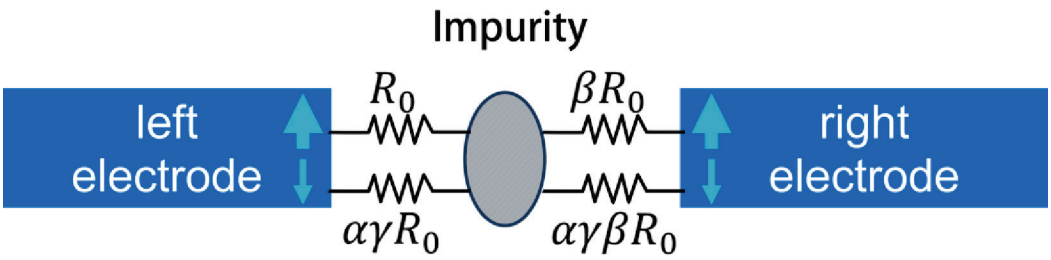

Figure A2.4

Schematic of the equivalent circuit diagram based on the model when the MTJ is in the P-state.

The Fano factors for spin up and spin down channels, $F_{\uparrow}$ and $F_{\downarrow}$ respectively, were computed by treating the system as a double tunnel junction; thus adopting the relatively well-known Fano factors for double tunnel junctions of two spin channel [1] we can write:

$$F_{\uparrow} = {(R_{\uparrow}^{left})^2 + (R_{\uparrow}^{right})^2}\Big/{(R_{\uparrow}^{left} + R_{\uparrow}^{right})^2} \text{ and } F_{\downarrow} = {(R_{\downarrow}^{left})^2 + (R_{\downarrow}^{right})^2}\Big/{(R_{\downarrow}^{left} + R_{\downarrow}^{right})^2}.$$

Finally the total Fano factor was given using:

$$F = \left(\frac{F_{\uparrow}}{R_{\uparrow}^{left}+R_{\uparrow}^{right}} + \frac{F_{\downarrow}}{R_{\downarrow}^{left}+R_{\downarrow}^{right}}\right)\Big/\left(\frac{1}{R_{\uparrow}^{left}+R_{\uparrow}^{right}} + \frac{1}{R_{\downarrow}^{left}+R_{\downarrow}^{right}}\right).$$

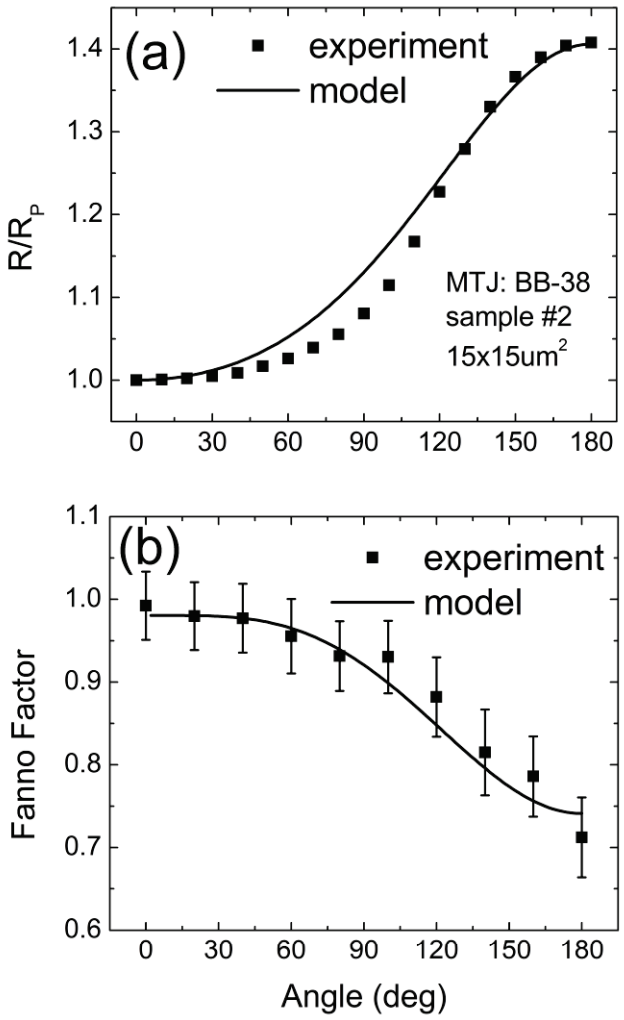

Figure A2.5

An example showing comparison between measurements (squares) and calculation (solid lines) using the model described in the text for angle dependent junction resistance (a) and Fano factor (b); parameter values α=20, β=100, γ=1.22 were used for modeling resistance and the Fano factor.

Besides the Fano factor, angle dependent normalized resistance (essentially TMR) can also be computed according to the resistor network of Fig.A2.4, and the results of resistance and the Fano factor as functions of angle are presented in Fig.A2.5. A

set of the parameters were used to fit both plots. A very asymmetric barrier configuration (β=100) was used, and the value of β critically determines the noise properties, both the value of the Fano factor and its angle dependence (i.e. in the limit β→0 or ∞, the impurity disappears and therefore F=1 independent of angle).

Though both resistance and shot noise from the impurity model agree fairly well with the experiments, we cannot exclusively conclude that this impurity model correctly explains the shot noise behaviors. Some open questions remain to be answered by young and ambitious physicists. For instance, in reference 3, a rather different result from ours, $1 \geq F_{AP} \geq F_P$, was found in Co/AlO_X/NiFe junctions. How can one understand the discrepancy? Also, having a single impurity site in the barrier seems to be oversimplified and unphysical. How do one account for a distribution of impurities across the barrier? If impurity sites do exist, what is their nature and are there any charge or spin restrictions that will affect the transport and noise? More importantly, are there other possibilities of explaining the suppression of shot noise in AP-state? Preparing the barrier differently and also studying the annealing effect could be effective ways to verify this impurity model. Furthermore, the equation for shot/Johnson noise, $S_V = 2eRV\coth(\frac{eV}{2k_BT})$ [2], was derived by assuming junctions having normal metal electrodes (flat DOS). This can be modified by incorporating the DOS of ferromagnets in order to study if the measured shot noise can be affected by the DOS features. One question leading to another and one adventure being followed many more, this is exactly how this ever vibrant and exciting subject of science keeps going and continues to thrive.

References

[1] Ya.M. Blanter and M. BuK ttiker, Physics Reports 336 (2000) 1-166

[2] G. Lecoy and L. Gouskov, Phys. Status Solidi 30, 9 (1968)

[3] R. Guerrero, F. G. Aliev, Y. Tserkovnyak, T. S. Santos, and J. S. Moodera, Phys. Rev. Lett. 97, 266602 (2006)

Appendix 3:
Supplementary Data for the Conductance Feature

1. Temperature dependence

The temperature dependent conductance was measured for two junctions using a Physical Property Measurement System, shown in Fig. A3.1. As the temperature goes down, the conductance feature around 250mV becomes more pronounced. The peaks in the density of states are temperature dependent, and one expects to see sharper peaks at lower temperature. The temperature also affects the tunneling conductance via the Fermi function; the primary contribution to the conductance is from the electrons within energy bandwidth of k_BT around the Fermi level. Therefore, the effect of raising the temperature is equivalent to smearing the density of states features by increasing the energy resolution bin size. However, the position of the conductance feature does not shift much with temperature.

Also, the dip at V=0 is a relatively well-known effect referred to as zero bias anomaly. It is caused by hot electrons exciting magnons at the interfaces [1], and it gets sharper with decreasing temperature.

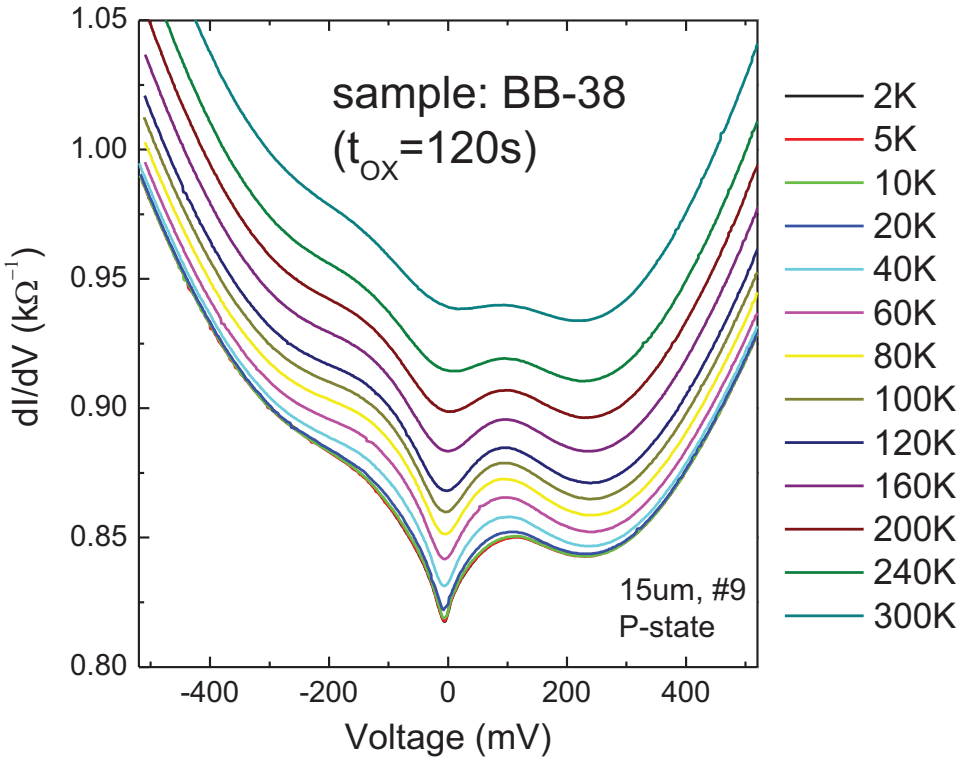

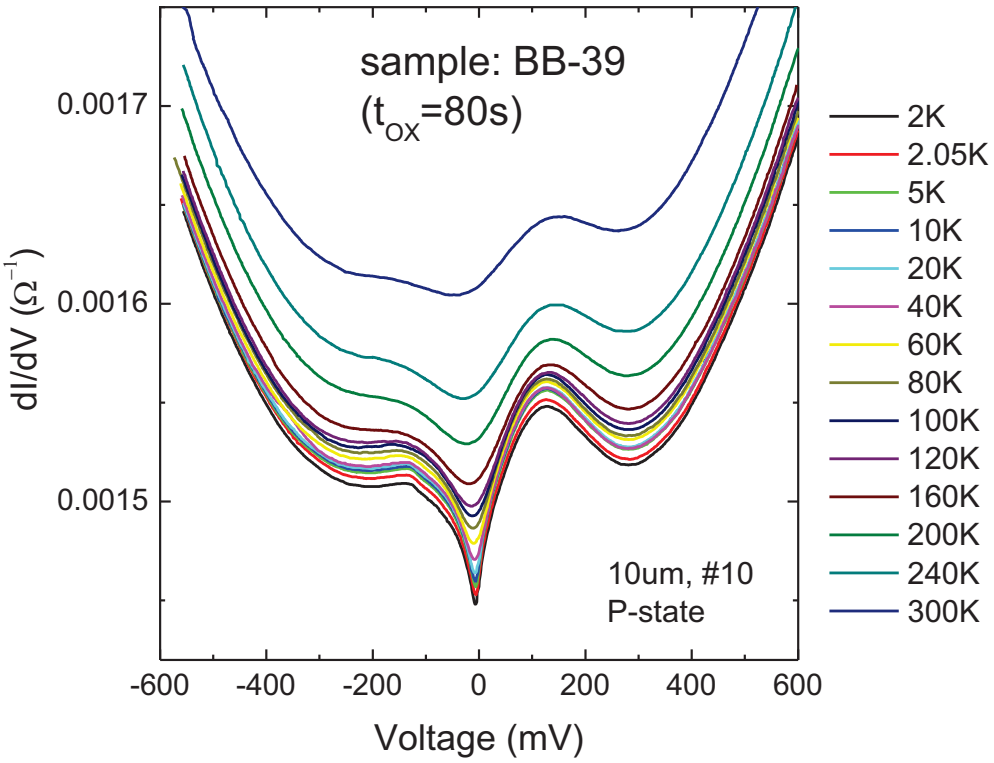

Figure A3.1

Two samples demonstrating the temperature dependence of dI/dV(V) in P-state.

2. TMR vs. V for wedged samples

A second set of aluminum wedge samples were made with TMR and RA vs. Al thickness and conductance curves similar to those in Figs. 3.8 and 3.9. TMR and the first derivative of TMR, d(TMR)/dV, are present in Figs. A3.2c and A3.2d. Note that the conductance feature also reveals itself in the plot d(TMR)/dV vs. V. Though noisy, one can still see the bump appears around 200-300mV where the conductance feature occurs.

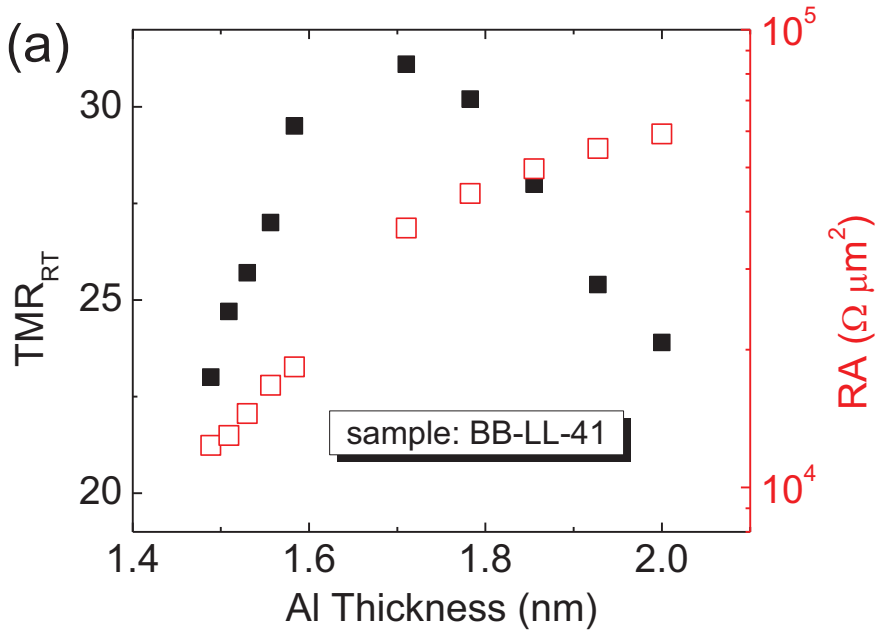

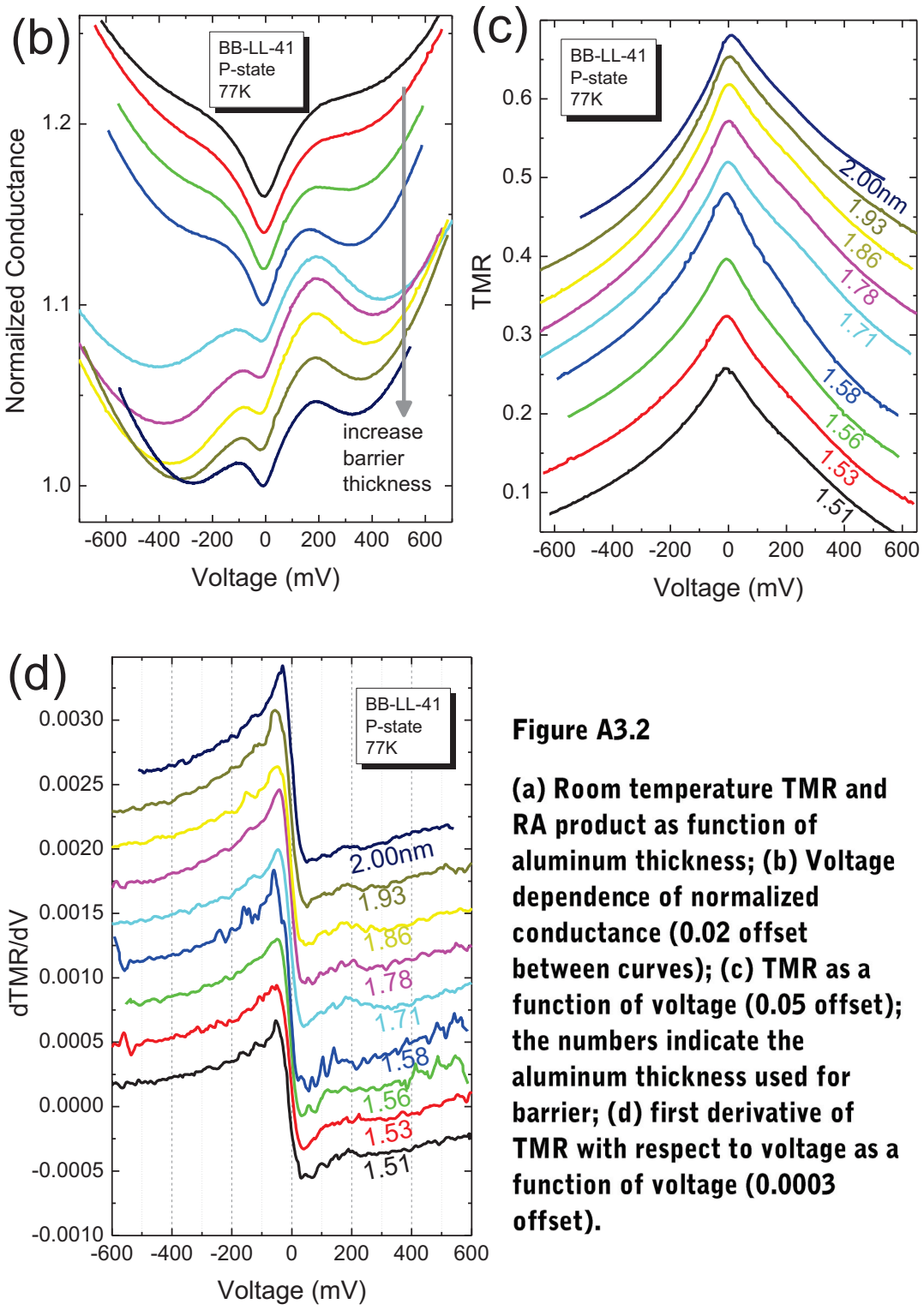

Figure A3.2

(a) Room temperature TMR and RA product as function of aluminum thickness; (b) Voltage dependence of normalized conductance (0.02 offset between curves); (c) TMR as a function of voltage (0.05 offset); the numbers indicate the aluminum thickness used for barrier; (d) first derivative of TMR with respect to voltage as a function of voltage (0.0003 offset).

References

[1] S. Zhang, P. M. Levy, A. C. Marley and S. S. P. Parkin, Phys. Rev. Lett., 79, 3744 (1997)

Appendix 4:

Basic theories of Tunneling Conductance

One simple approach to quantitatively calculate the tunneling current of a MTJ can be described by the following equation:

$$I \propto \int_{-\infty}^{\infty} eN\{f(E-eV)-f(E)\}T(E)^2 dE,$$

where ***e*** is electron charge; ***N*** is a function referred to as the effective density of states which contains the density of states for the two electrodes as discussed below; the Fermi function ***f*** is defined as $f(E) = 1/[e^{(E-E_F)/k_BT} + 1]$; the tunneling probability T^2 is computed using WKB approximation for simplicity:

$$T(E)^2{}_{WKB} = e^{\frac{-2}{\hbar}\int_0^d \sqrt{2m(\phi(x)-E)}dx},$$

in which ***m*** is the electron mass, and ***ø*** and ***d*** are the barrier energy height and width respectively.

For non-magnetic junctions the effective density of state, ***N***, is the product of densities of states of the left and right electrodes, and in MTJs it depends upon the magnetization orientations and is defined as follows:

For the parallel state:

$$N_{\uparrow\uparrow} = D_{\uparrow}^{left}(E - eV)D_{\uparrow}^{right}(E) + D_{\downarrow}^{left}(E - eV)D_{\downarrow}^{right}(E);$$

and for the anti-parallel state:

$$N_{\uparrow\uparrow} = D_{\uparrow}^{left}(E - eV)D_{\downarrow}^{right}(E) + D_{\downarrow}^{left}(E - eV)D_{\uparrow}^{right}(E).$$

The tunneling current as a function of voltage can be computed using the equations above and the differential conductance can be obtained by taking the derivative of the current-voltage curve. In order to see how the density of states effect plays a role in the conductance, we artificially created the densities of states shown in Fig.A4.1. On top of the flat density of states background, two identical peaks, one at 0.6V below the Fermi level and the other 0.3V above the Fermi level, were generated either in the majority spin band or the minority spin band shown in Figs.A4.1a and A4.1d respectively. A completely flat density of states was used for the other electrode. Positive voltage was defined for electrons flowing from the density of state with peaks to the flat one. As one can see from Figs.A4.1c and A4.1f, all the peaks in the density of states individually give rise to the peaks in the conductance, and the locations of these peaks are consistent between the density of states and the conductance as expected.

Several interesting features are found in this calculation. For the case of the peaks located in majority band, the peak in the parallel state is always stronger than the one in the anti-parallel state (also at the same location); the can be simply understood from the equations:

$N_{\uparrow\uparrow} = D_{\uparrow}^{peak(left)} D_{\uparrow}^{flat(right)} + D_{\downarrow}^{flat(left)} D_{\downarrow}^{flat(right)}$ and

$N_{\uparrow\downarrow} = D_{\uparrow}^{peak(left)} D_{\downarrow}^{flat(right)} + D_{\downarrow}^{flat(left)} D_{\uparrow}^{flat(right)}$.

Since $D_{\uparrow}^{flat(right)} > D_{\downarrow}^{flat(right)}$ and whenever $D_{\uparrow}^{peak(left)}$ which carries the peak information times a bigger number will give a peak having a larger magnitude in the conductance, the peak in the parallel state is thus bigger than that in the anti-parallel state. As a second conclusion from the calculation, the peak height is strongly position dependent. The peak in the density of states having a higher energy always gives a stronger peak in the conductance, i.e. the DOS peak at 0.3V leads to a much stronger conductance peak than the one at -0.6V; this is because the electrons from the DOS with higher energies see a lower barrier height and the tunneling probability for these electrons is lower, resulting to stronger conductance features. Similarly, the DOS peaks located at lower energies give less pronounced conductance peaks.

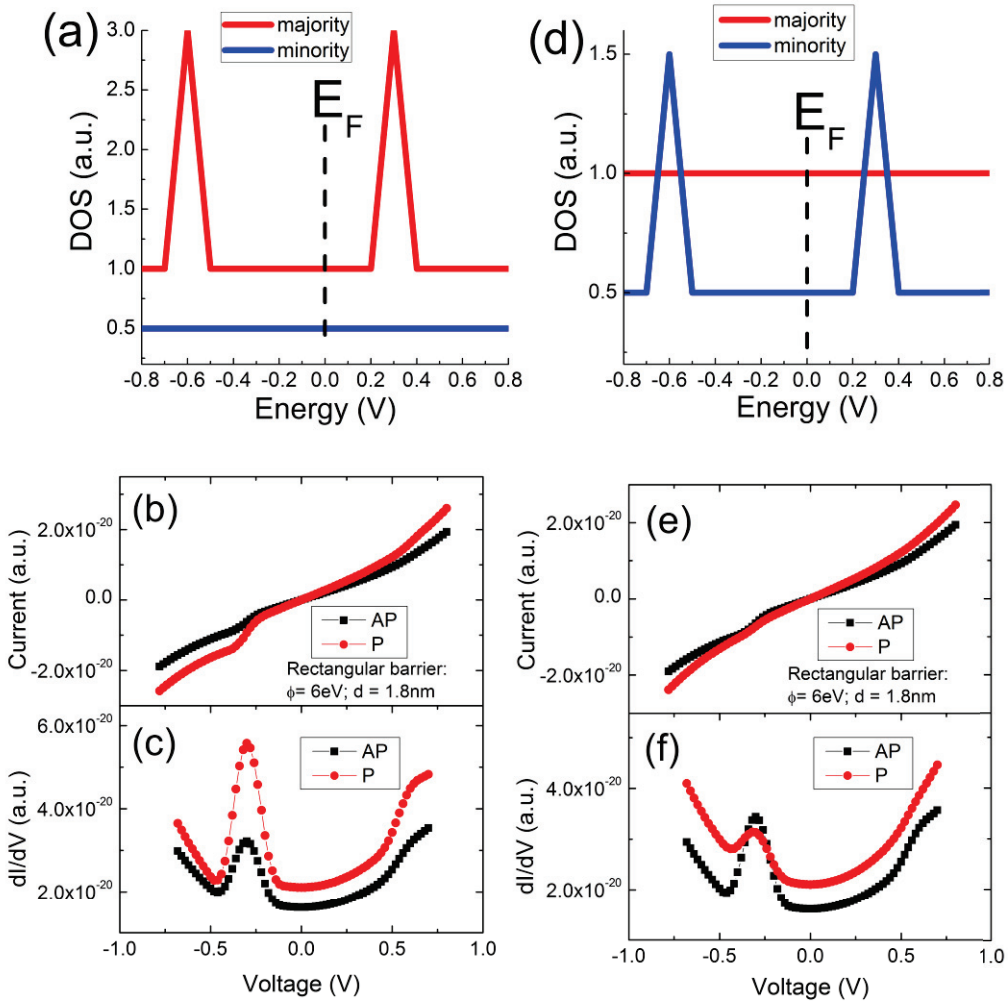

Figure A4.1

(a) Density of states consisting of two peaks (-0.6V and 0.3V) in the majority band and flat backgrounds; I-V curve (b) and dI/dV vs. V (c) using the density of states in (a) and completely flat density of states for the other electrode; (d-f) same set of calculation as (a-c) except the peaks are in the minority band.

For the density of states with peaks in minority spin band, the DOS peaks are also reflected in the conductance curves. The conductance peaks at -0.3V and 0.6V

correspond to the DOS peaks at 0.3V and -0.6V respectively, and the -0.3V peaks are stronger than those at 0.6V. However, opposite to the previous case, the peaks in the anti-parallel state have bigger amplitudes than those in the parallel state, for the similar reason discussed above.

Bias dependent TMR ratios were also calculated for the two cases (Fig.A4.2). If a flat density of states was used for both electrodes, the TMR would be independent of voltage. Nevertheless, due to the difference in peak strength in different magnetic state, the MTR ratio was found to be instead voltage dependent at the voltages where the peaks are present. For the case where the majority density of states containing the peaks, the TMR will be enhanced at the peak locations, and the higher energy the DOS peak has the bigger effect it will carry into the TMR. For example, as one can see in Fig.A4.2a the bump at -0.3V is much more pronounced than the one at 0.6V. For the peaks present in minority band, the TMR ratio will be instead suppressed at the peak locations, shown in Fig.A4.2b.

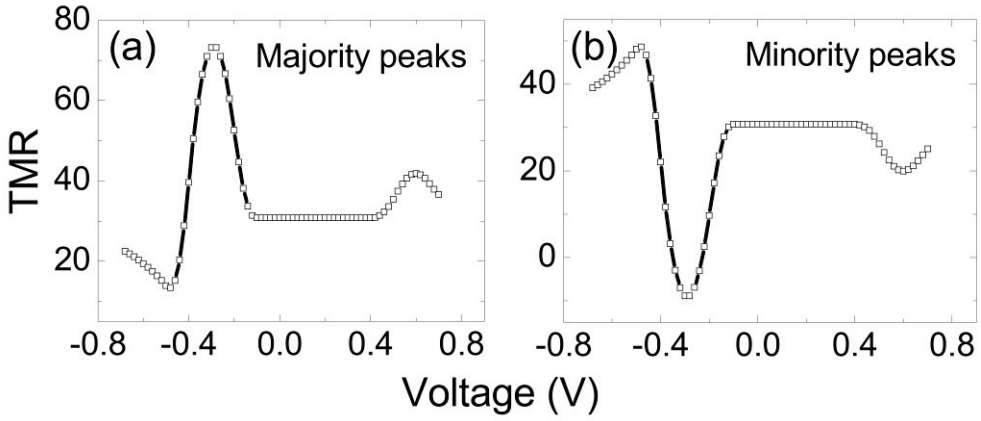

Figure A4.2

Panels (a) and (b) show the bias dependent TMR computed from (c) and (f) respectively.

Though may be oversimplified, this conductance calculation demonstrates a good and simple example of how the density of states plays a role in MTJ conductance.